AES/TGP/11-30

High Resolution VSP Detection of Point Bar Structures within Bituminous Sands

25-08-2011

Mengmeng Zhang

Department of Geotechnology

Delft University of Technology

Title : High Resolution VSP Detection of Point Bar Structures within Bituminous Sands

Author(s) : Mengmeng Zhang

Date : August 2011
Professor(s) : Prof. dr. ir. C.P.A. Wapenaar
Supervisor(s) : Dr. Steen Agerlin Petersen
TA Report number : AES/TGP/11-30

Postal Address : Section for Applied Geophysics and Petrophysics
Department of Applied Earth Sciences
Delft University of Technology
P.O. Box 5028
The Netherlands
Telephone : (31) 15 2781328 (secretary)
Telefax : (31) 15 2781189
Electronic-mail : michaelzhang95@gmail.com

High Resolution VSP Detection of Point Bar Structures within Bituminous Sands

Master of Science Thesis

For the degree of Master of Science in Applied Geophysics

Mengmeng Zhang

August 2011

TU Delft

Delft
University of
Technology

Abstract

The connectivity between SAGD pair-wells is the key for success of SAGD processes. The bituminous sands of Corner field situate in middle McMurray, where tidal influenced meandering fluvial point bar dominate the deposits. Thus, to characterize the internal structure of point bar deposit is essential to optimize SAGD production in Corner field.

The aim of this thesis is to investigate correspondences between point bar internal structures and VSP responses. Since VSP preserve higher frequency than surface seismic thus VSP data would provide more precise identification and characterization of internal structures if we can recognize them from data. These investigations are done by comparing actual data, synthetic data and targets part in the model.

Prior to the comparisons, we need to build a model that preserves the characteristics of our targets in subsurface as accurate as possible. We decompose the segment of logging data corresponding to the thickness of point bar deposits into a function which is able to represent the influence of gravity on deposition and a function that is able to imply the affect of current. After examining geometrical relation between borehole and inclined units of point bar structure, two scaled functions combine in a way that result in structures of point bar deposits.

As soon as a realistic model is constructed, VSP simulations proceed. Based on the comparison of plane wave source VSP data with the model, it is found that variation of travel-time difference between two levels indicate heterogeneities between these levels.

Since finite difference used in this thesis is based on acoustic wave propagation, only travel-time is investigated. While if an elastic modeling is available, the results will be more fruitful with respect to amplitudes variation and wave conversion.

Acknowledgement

This thesis would never be complete without acknowledging Steen Agerlin Petersen, who is a better supervisor than any graduate student could ever wish for. I am grateful that Steen expressed his confidence in me by suggesting such a challenging and interesting topic and guided me throughout the thesis work. I would also like to show my gratitude to my colleague Thomas Greig for his assistance in providing references of study area. I express my thanks to Statoil ASA for providing research facility and accommodation in Bergen. And of course, thank you Mom and Dad, for your understanding, support and encouragement.

Mengmeng Zhang
Bergen, Norway
August 2011

Table of content

Nomenclature

VSP	Vertical Seismic Profiling
SEMs	Shared Earth Models
PSDM	Prestack depth-migrated seismic
SAGD	Steam Assistant Gravity Drainage
IHS	Inclined Heterolithic Strata
IS	Incline Strata
BPF	Borehole Property Function
BVF	Borehole Variation Function
IPF	Property Function along Inclined units
IVF	Variation Function along Inclined units
HMI	High resolution Micro Imager log

Chapter 1

Introduction

1.1 Rationale

Alberta's bituminous sands account for a large amount of hydrocarbon deposit in the world, and over 80% of them are buried deep below the earth's surface. In order to recover these resources, in-situ recovery techniques are needed. Steam Assistant Gravity Drainage (SAGD) is one of the advanced oil recovery technologies. By situating two parallel horizontal wells deep underground, steam is injected into the shallower one, the heat lowers the viscosity of bitumen, which then flows downward to the deeper producing well. From there, the bitumen is extracted to the surface.

As heating, mobilizing and flowing are core procedures for SAGD, the continuity between SAGD well-pair is a preliminary condition for the success of SAGD processes. In our area of investigation (Corner field), bitumen is mainly located in middle McMurray, where tidal influenced meandering fluvial point bar dominate the deposits. Therefore, in order to optimize SAGD process, internal structures of point bar deposits in the reservoir need to be investigated in detail, which surface seismic alone does not always provide enough information. Thus mapping must be considered as a joint effort of surface seismic and other borehole information.

The aim of this thesis is to investigate VSP responses related with internal structures of point bar deposits, by simulating a variety of acquisition layouts. However, a near-to-realistic model, as a preliminary part, should be constructed before VSP simulation can be proceeded.

1.2 Outline of the thesis

Chapter 2 presents backgrounds of this study including regional geology and depositional processes and a brief introduction of Steam Assistant Gravity Drainage (SAGD) processes. Chapter 3 briefly describes the principles used in our model construction and simulation. In chapter 4, an innovative method is developed by which realistic property distributions of inclined heterolithic strata (IHS) deposits are created. The IHS model forms the basis for the surface seismic simulation (this chapter) and subsequent VSP simulations. In chapter 5, synthetic zero-offset VSP data are created and compared with actual data to try to identify point bar structures in VSP data. Chapter 6, offset and plane wave source with receivers laterally distributed VSP data are evaluated and compared with velocity model, then end up with acoustic model based conclusions of relation between travel-time and point bar internal structures. Recommendations and comments follow in chapter 7.

Chapter 2

Background of study area

Alberta's bituminous sands is one of the largest hydrocarbon deposits in the world, and most of them are located in three main areas of northeastern Alberta: Cold Lake, to the south; Peace River, to the west; and Athabasca, to the north. (Figure 2.1). Of these deposits, Athabasca is the largest, in which Corner field is located. In this chapter, a brief description of regional geological settings of our interested formations is given first. Then we focus on our study area – Corner field, concisely describe the local deposition faces, geomorphology, and exploration history. At the end of the chapter, an in-situ thermal enhanced oil recovery technology for bitumen is succinctly described.

2.1 Regional geology[1]

2.1.1 Stratigraphy

The Manville group (and equivalents) comprise the oldest Cretaceous rocks in the Western Canada sedimentary basin and represent a major episode of sedimentation following a period of uplift, exposure and erosion of older strata. In northeastern Alberta,

---

[1] This part is an extract from Master DG2 Geosciences documentation (Statoil internal document), by Diakiw G., Greig T., Hoehn, M., Jordan, O., Brekke, H., 2011

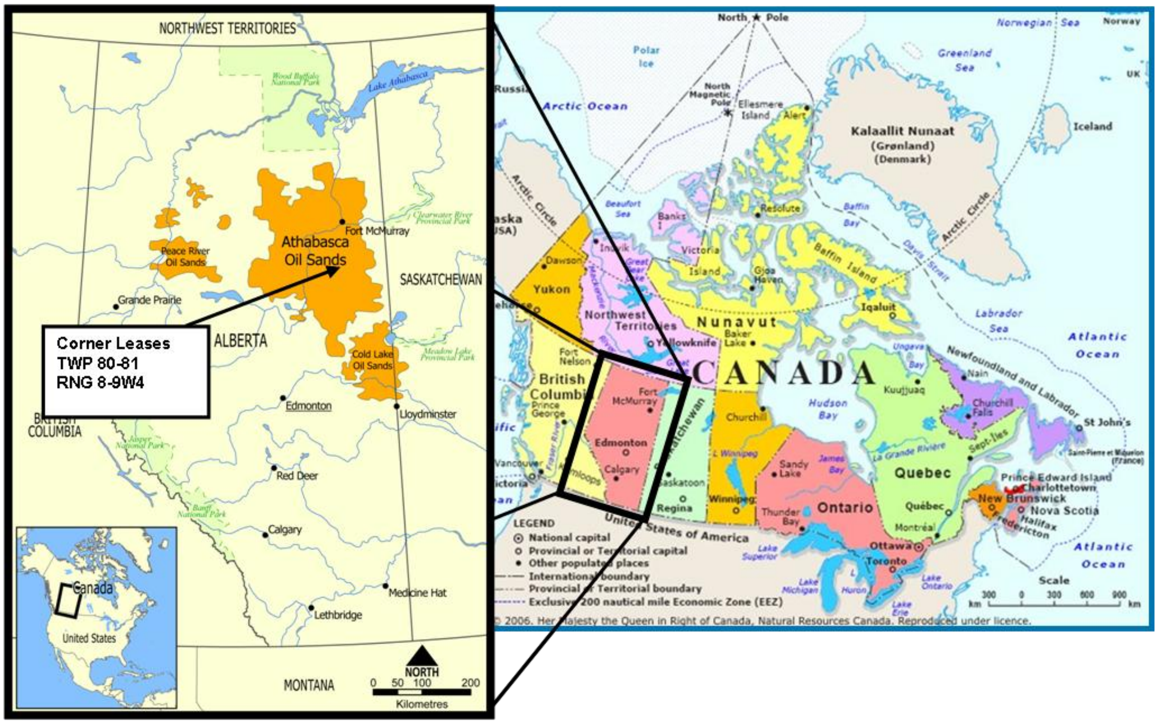

Figure 2.1: Map of Alberta with main bituminous sands distribution and approximate location of the Corner Area [Diakiw G., Greig T., Hoehn, M., Jordan, O., Brekke, H., 2011].

the Manville Group is composed primarily of unconsolidated clastic sedimentary rocks which are divided into three formations. From oldest to youngest, these formations are the McMurray Formation, the Clearwater Formation and the Grand Rapid Formation. Of these formations, the most of interest is the McMurray Formation within which the bitumen resource located. The McMurray Formation overlies a major erosional unconformity which separates the McMurray Formation from the underlying Devonian Carbonates units. The unconformity is formed during a period of sub aerial exposure and erosion which results in distinctly incised valleys that influence the deposition of McMurray Formation.

The McMurray Formation has been sub-divided into three units, namely the lower, middle and upper McMurray. The lower McMurray deposits in fluvial environment, while the middle McMurray sediments are deposited in fluvial-estuarine point bar systems. The upper McMurray deposits in estuarine and interdistributary bay environments. Figure 2.2 depicts a simplified schematic stratigraphic model. The approximate location of the stratigraphic section is indicated as the black line on the

Figure 2.3 which shows main depositional events of the Corner area within McMurray formation. (The main depositional events will be described in 2.1.2).

The Corner area contains isolated units of the lower McMurray, normally located in topographic lows of the underlying Devonian carbonate. The middle and upper McMurray units are comprised of a complex variation of facies types, but typically dominated by relatively clean channel sandstones (good reservoir), interbedded heterolithic sandstones and mudstones (good to poor reservoir) and mud stones (poor reservoir). The majority of deposition is associated with point bar accretion which results in a significant proportion of deposition dominated by inclined heterolithic stratification (IHS). Bitumen reservoir are mainly formed in the middle and upper McMurray, therefore, significant heterogeneities of reservoir, which result from high complexity of IHS, lead to great challenge of bitumen production.

2.1.2 Geological settings of the Corner Field

The Corner Field can be divided into two regions: the Main pool and the Northwest (NW) pool, shown in Figure 2.3. We only present depositional events within our interest formation – McMurray. Generally, there are three big point bar systems and several related abandonment channels developed in the formation. According to Diakiw et al. (2011), during Middle McMurray, as sea level dropped, a northward prograding point bar develops, shown in Figure 2.3 labeled by point bar A. This point bar does not contribute to the deposition of the bitumen reservoir in its developed area, since it is eroded by the following east to west flowing channel system in southern part of Main pool, which results in deposition of point bar B. At a later time, the point bar B is incised and partly eroded by a southeastwards migrating point bar originated in the Northwest pool of the Corner area, which is labeled by point bar C. As shown in Figure 2.3, abandonment fills associated with point bar migration also presents in both pools.

2.1.3 McMurray depositional process in NW pool

The primary purpose of this study is to investigate special VSP responses related with IHS structures, so the complex IHS construction is the preliminary part of this study. From surface seismic slices, NW pool presents more pronounced scroll patters, which are typical seismic features of point bar deposits, than Main pool does, therefore we choose NW pool as our study area.

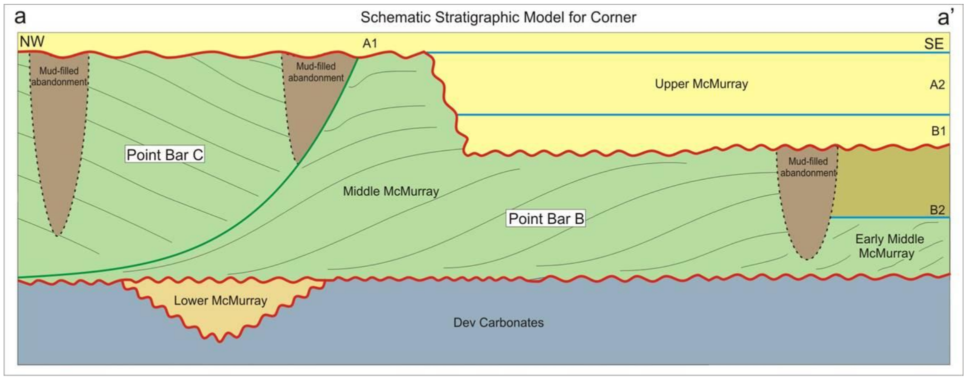

Figure 2.2: Schematic stratigraphic model of Corner area. [Jordan and Hoehn after Brekke and Roenitz, 2010]

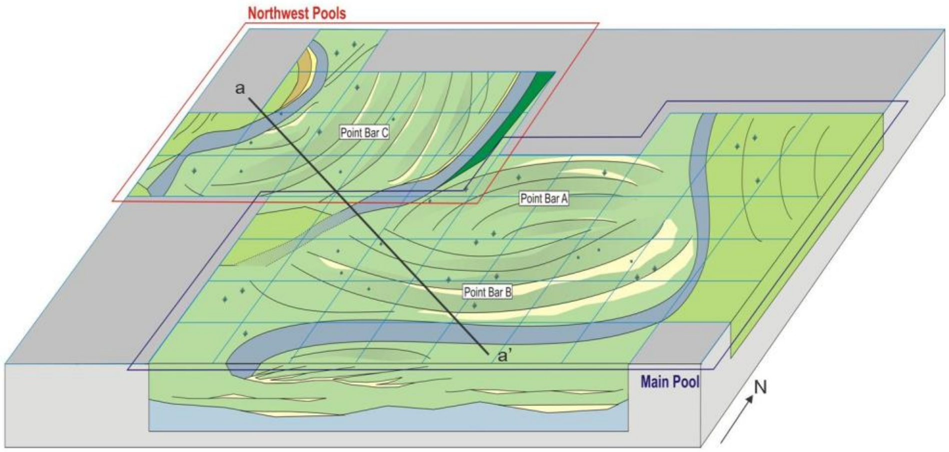

Figure 2.3: Schematic conceptual geological model with main depositional events in McMurray formation of the Corner area. [Jordan and Hoehn after Brekke and Roenitz, 2010]

Diakiw et al. (2011) described that lower McMurray units in NW pool exhibit complex depositional pattern, shown in Figure 2.4 with red arrows of little organization, which represent dip data. These unorganized dipping patterns result from the complex Devonian topography on which basal facies are deposited and are considered as part of the Lower McMurray. The Middle McMurray can be subdivided to two units. The lower part of Middle McMurray is highly organized and forms the bulk of the units in NW pool. It was deposits by the migration of point bar C (Figure 2.3) and pronounced scroll patterns can be observed in seismic time slice (Figure 2.8). This point bar C migrates southeastwards and deposits highly variable architecture of channel sandstones, inclined heterolithic strata and abandonment mudstone fills (the top diagram of Figure 2.4). The upper part of Middle McMurray exhibits two channel systems (two blue channels show in the bottom diagram of Figure 2.4) which are also definable from seismic slice (Figure 2.9). Then the Middle McMurray is truncated by an erosional unconformity which covers the entire northwest region and overlain by late Upper McMurray (Figure 2.2).

2.2 Geophysical data in Corner area

The Corner area has been covered by a large range of geophysical data [Figure 2.5], including merged 3D seismic throughout the entire area, approximate 270 wells drilled with standard log suite, many of them have core and/or high resolution micro imager logs (HMI). Besides wireline logging data, 4 checkshots and 4 zero-offset VSP have been acquired in selected wells.

Figure 2.6 is a seismic depth slice at Devonian Top, which presents highly sinuous channel systems in NW pool. I choose a subarea in NW pool as the study area which contains a big channel system, with the size of 5600m ×5600m and grid space of 28m ×28m. After looking through different depth slices, in order to preserve relative more pronounced IHS features in a selected seismic section, I pick a line almost along the direction of point bar lateral accretion, i.e., cutting through scroll patterns almost perpendicularly on average [Figure 2.8 and Figure 2.9]. The seismic section is shown in Figure 2.7. There are seven wells near the selected seismic line, which are used to control our model [Figure 2.10]. It is interesting to notice that the direction of scroll patterns intersecting with our selected profile shown in Figure 2.10, which represent deposits of the Lower McMurray in the sinuous channel, is slightly different with that shown in Figure 2.8, which represents sediments of the Middle McMurray.

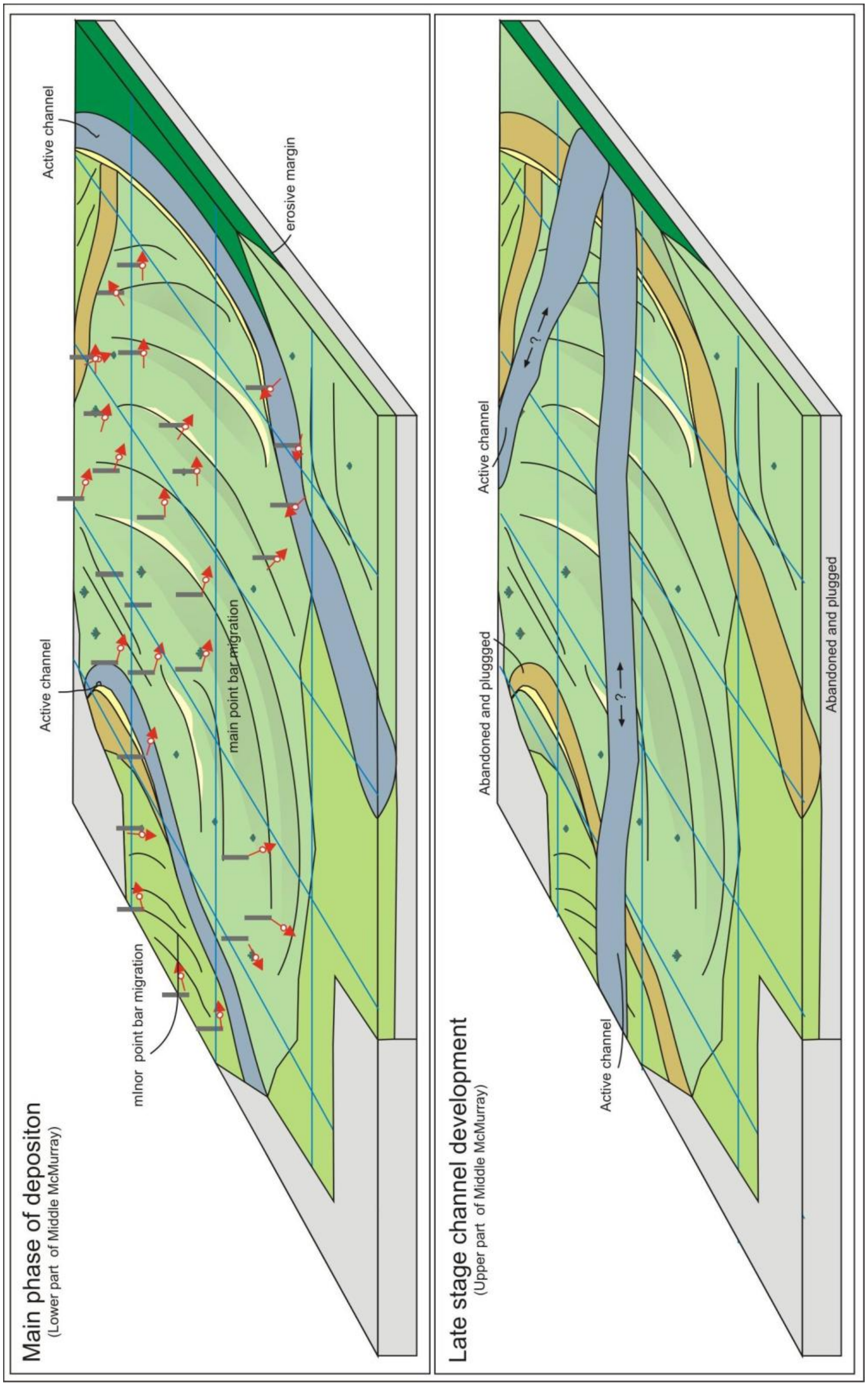

Figure 2.4: Schematic conceptual model of two deposition stages in Northwest pool of Corner area [Jordan and Hoehn, 2010].

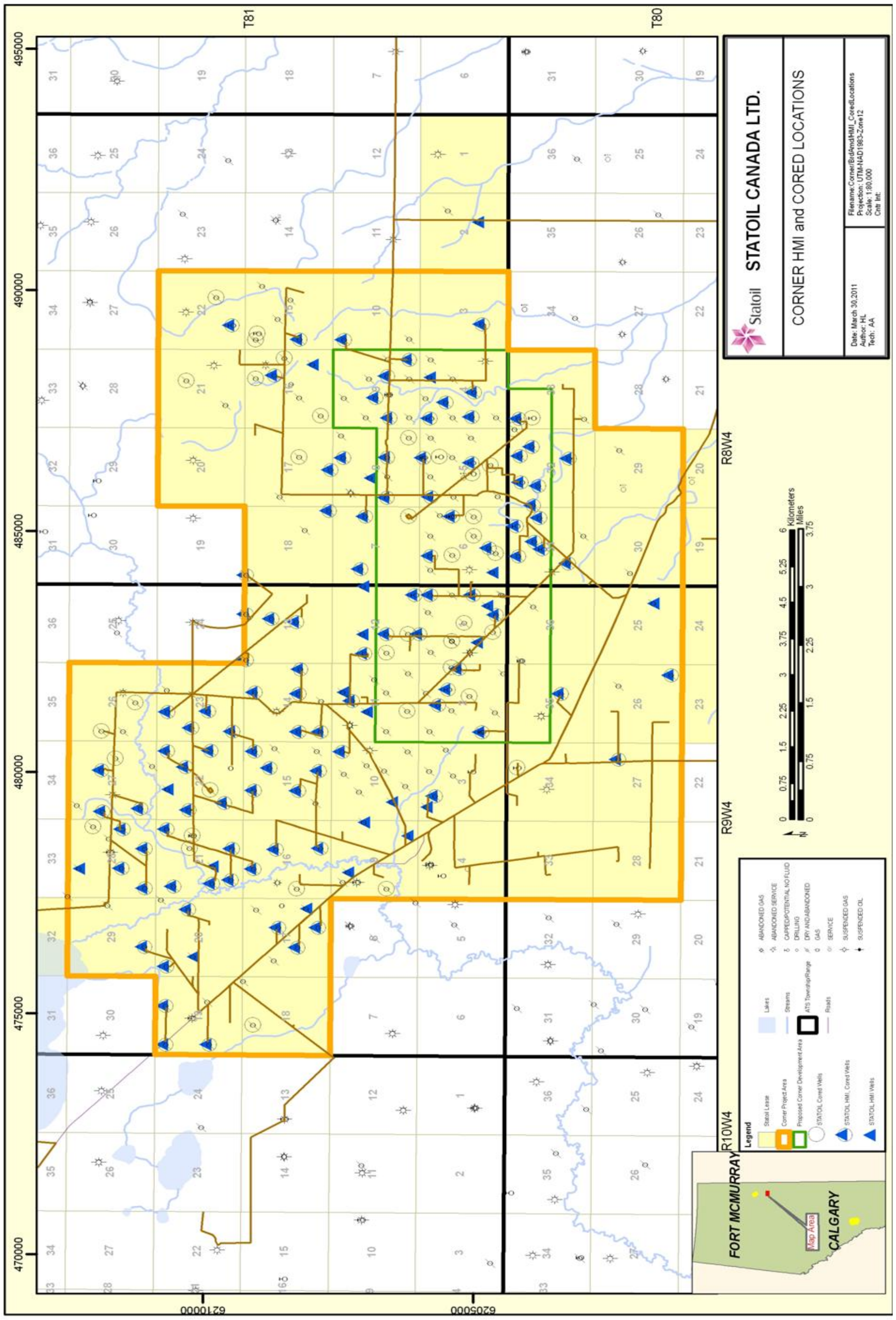

Figure 2.5: A map of geological and geophysical control for Corner area, and it illustrates distribution of wells with cores or/and HMI data. [Statoil Canada Limited, DG2 group]

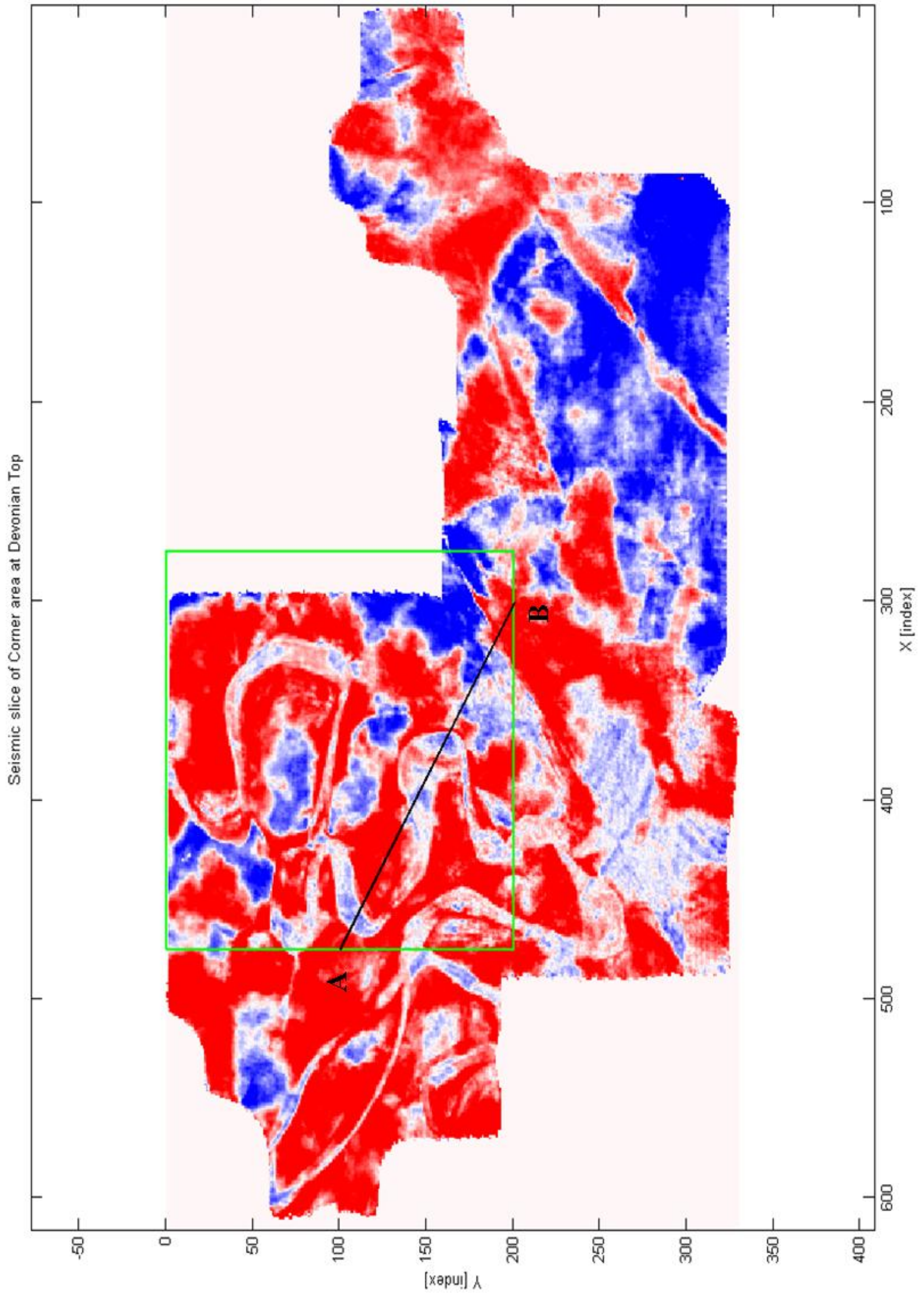

Figure 2.6: Seismic slice of corner area at Devonian top, presents significant meandering channels incised in Devonian top, the green frame indicate the study area, and black line indicate the selected seismic profile based on which the model will be built.

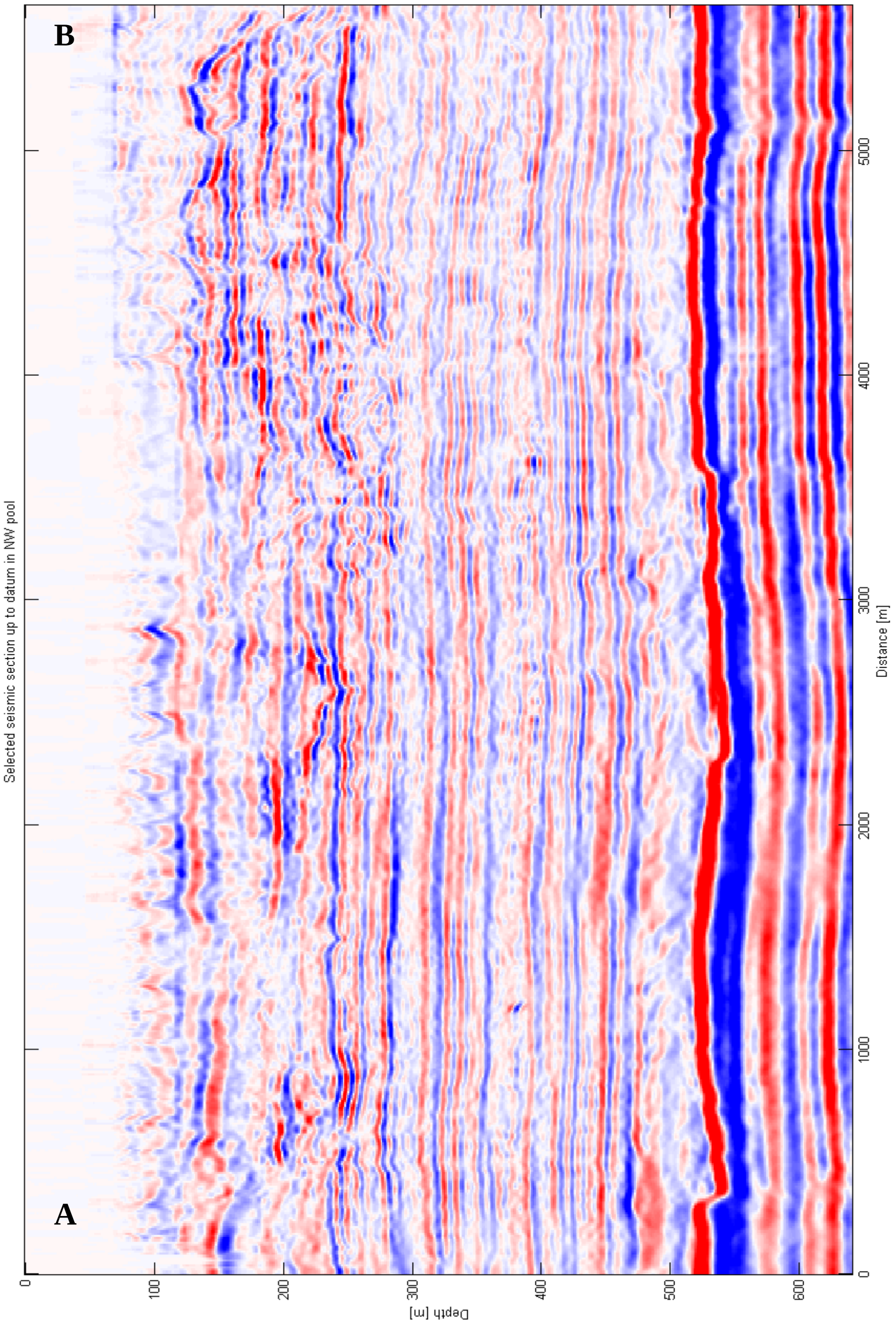

Figure 2.7: Surface seismic section along the selected line, the depth is relative to surface seismic reference level.

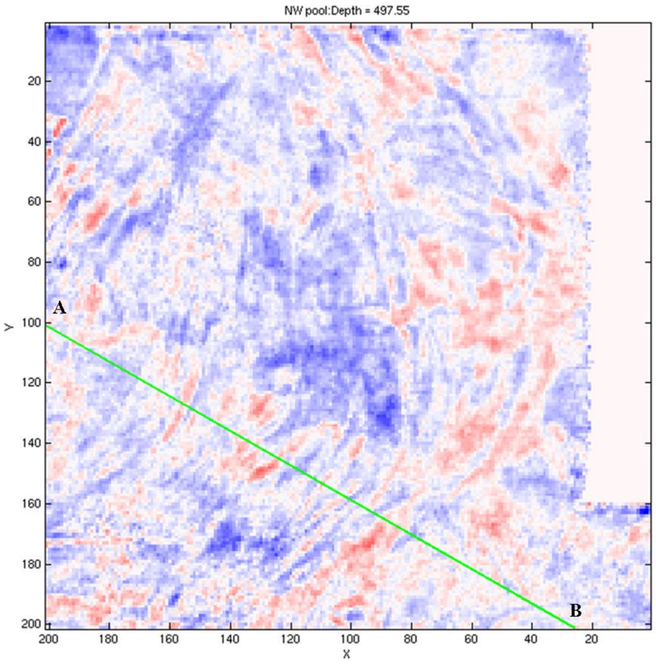

Figure 2.8: NW pool, Seismic slice at depth of 497.55m (relative to surface seismic reference level) with indication of selected seismic profile and pronounced scrolls bars presenting lateral migration of point bar.

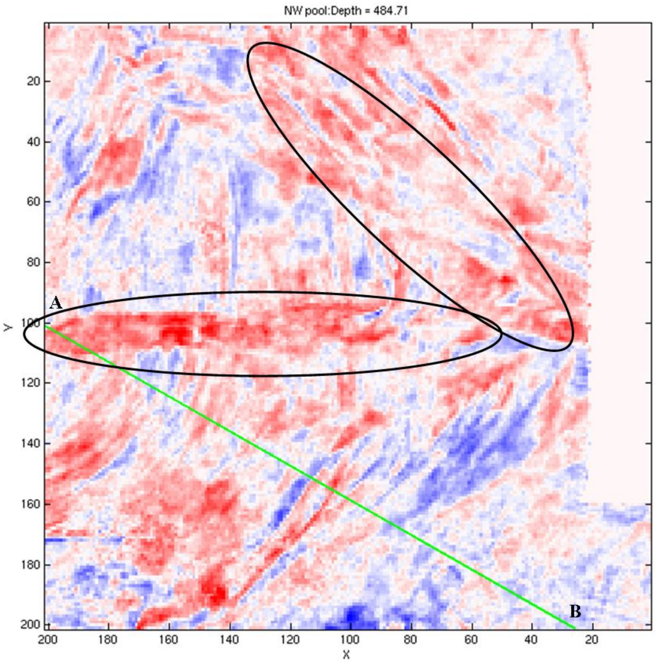

Figure 2.9: NW pool, seismic slice at depth of 484.71m (relative to surface seismic reference level) showing two channel systems in upper part of Middle McMurray, indicated in two ellipses.

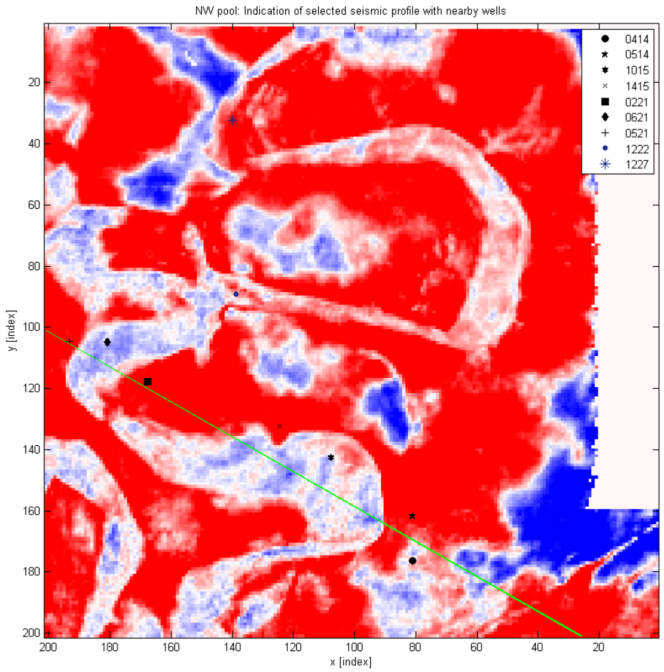

Figure 2.10: Depth slice shows relative positions of selected seismic profile and controlling wells.

2.3 Steam Assistant Gravity Drainage (SAGD)

Steam Assistant Gravity Drainage or SAGD is a thermal in-situ enhanced oil recovery technology for producing heavy oil and bitumen. It is an advanced form of steam stimulation in which two vertically aligned horizontal wells are drilled into the reservoir with a length of 700-1100m and vertical separation of 5m. The upper well (injection well) is used to inject steam to heat and mobilize bitumen and allow them to flow down to the lower well (production well) which collects and returns the oil and condensed steam to surface.

The SAGD process can be divided to preheat, SAGD production stage and blowdown three phases[1]

---

[1] The following paragraphs is an extract from: Leismer Demonstration Project SAGD Summery & Overview, Statoil Canada Limited.

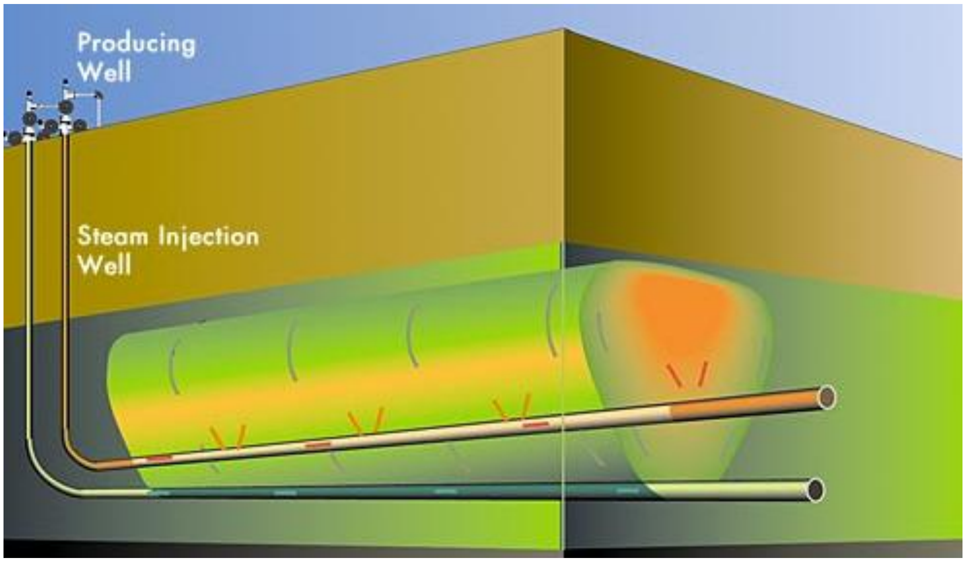

Figure 2.11 Diagram showing a pair of SAGD wells.

Preheat stage

The objective of the preheat phase is to heat the reservoir between the producer and injector so that heated bitumen has a path to drain down to the producer well. Both producer and injector are completed with tubing to the toe of the well for injection and a short tubing at or closer to the heel of the well for return. Steam is injected down to the toe tubing string and returns back to the heel tubing along the annulus (due to little or no mobility of highly viscous bitumen, steam have to be circulated in the well), transferring heat to the reservoir as condenses to liquid hot water. Well-based steam circulation will continue till the bitumen between the producer and injector has been mobilized and the wells are in communication, when the SAGD production phase can begin.

SAGD production stage

Before SAGD production phase starts, the producer well’s circulation tubulars have to be removed and replaced with a downhole pump to lift mobilized bitumen and hot water. As the bitumen’s temperature rises, its viscosity decreases and it becomes mobile and is able to drain downwards with condensed hot water to the producer via the 5m pathway created during the preheat stage. The drained oil leaves open pore space in reservoir rocks that can be then filled by steam, which result in the steam chamber growing vertically and laterally until its connecting with chambers from neighboring well-pairs.

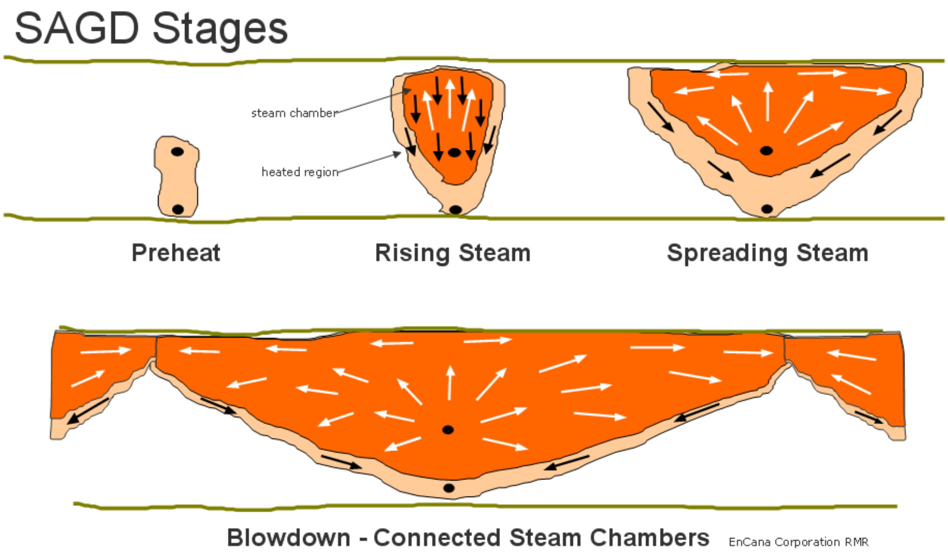

Figure 2.12: Schematic diagram of different SAGD stages with fluids' moving directions in every stage. White arrows indicate steam, and black arrows represent mobilized bitumen and condensed steam.

Blowdown stage

The blowdown stage is the last phase of SAGD, it is started as soon as the steam injection is stopped, however oil production can continue, though at a much higher decline rate. The well will be shut in when it is no longer economic to continue production.

Considering heating, mobilizing and flowing as core for SAGD, the continuity of reservoir between SADG well-pairs is a preliminary condition for the success of SAGD processes. While within McMurray Formation, the continuity is highly influenced or even controlled by IHS patterns presenting with interbedded sandstone and mudstone.

1

16

1

Chapter 3

Methodology

In this chapter, main methodologies of our model building and seismic simulation in are described. First, I present a short review of shared earth model and introduce a model builder – Compound DDrx (r – recursive, x - experimental) – which has been developing in Statoil ASA. Then principles of simulated migrated seismic is given, based on which surface seismic simulation implement in Compound DDrx. After that, finite difference modeling is briefly discussed, which is applied for Vertical Seismic Profile (VSP) forward simulation in chapter 5 and chapter 6.

3.1 Shared earth model and Compound model builder

If a model satisfies diverse sets of observations and includes additional constraints (geological) which reflect different aspects of the subsurface, we could say those observations and/or constraints 'share' the same model [S. A. Petersen, 2004]. Shared Earth models (SEMs) integrate and incorporate various types of observation to define subsurface property distribution.

A Compound DDrx model is based on sets of property, geometrical and logical entities. Property entities are made of distance dependent (1D) property functions which can be any physical property varying along any direction, e.g. logs of gamma ray, acoustic velocity and bulk density etc. are property functions along a well direction. Property entities are combined with geometrical entities (surfaces in 3D, curves and points in 2D or 3D) by distance field in order to create a spatial property distribution (a formation). Petersen et al. (2007) presented a methodology and implementation for fast creation of distribution in any spatial dimension and of any geological complexity by combination of distance fields from simple geometries and 1D distance dependent property functions. A formation then can be delimited by additional geometrical entities which indicate geological constraints, and it is a basic logical entity to constitute a hierarchy in which formations were ordered chronologically, for instance a younger formation overprints an older formation. In the same way, a hierarchy can be assigned by a delimiting geometrical entity as well and be ordered into higher 'super-hierarchy' and so on [S. A. Petersen, 2006].

According to how distances are calculated, spatial distribution can be sorted into three categories, which reflect different structural deformation styles. If distances relative to a geometrical entity are measured along a fixed direction, the distribution will reflect a similar structural deformation style. If distances are measured in terms of shortest paths from target points in space to a geometrical entity, the distribution will reflect concentric structural deformation style. The last style is the mixture of these two, which represents common type of deformations in the nature.

In addition, entity and hierarchy can also be reshaped or rotated by mapping relevant geometries to new reshaped or rotated ones, while these reshaping and/or rotating could represent geological and tectonic events occur after the formation(s) formed. A comprehensive overview of Compound model builder is referred to S. A. Petersen (1999 and 2006) and Petersen et al. (2007).

3.2 Principle of Simulated migrated seismic (SMS)

Seismic simulation is an important process during a forward problem. By comparing resultant synthetic data with real data, it helps geoscientists to identify special seismic events and relate them with geological features, to predict how variations in a geological setting might appear on a seismic image.

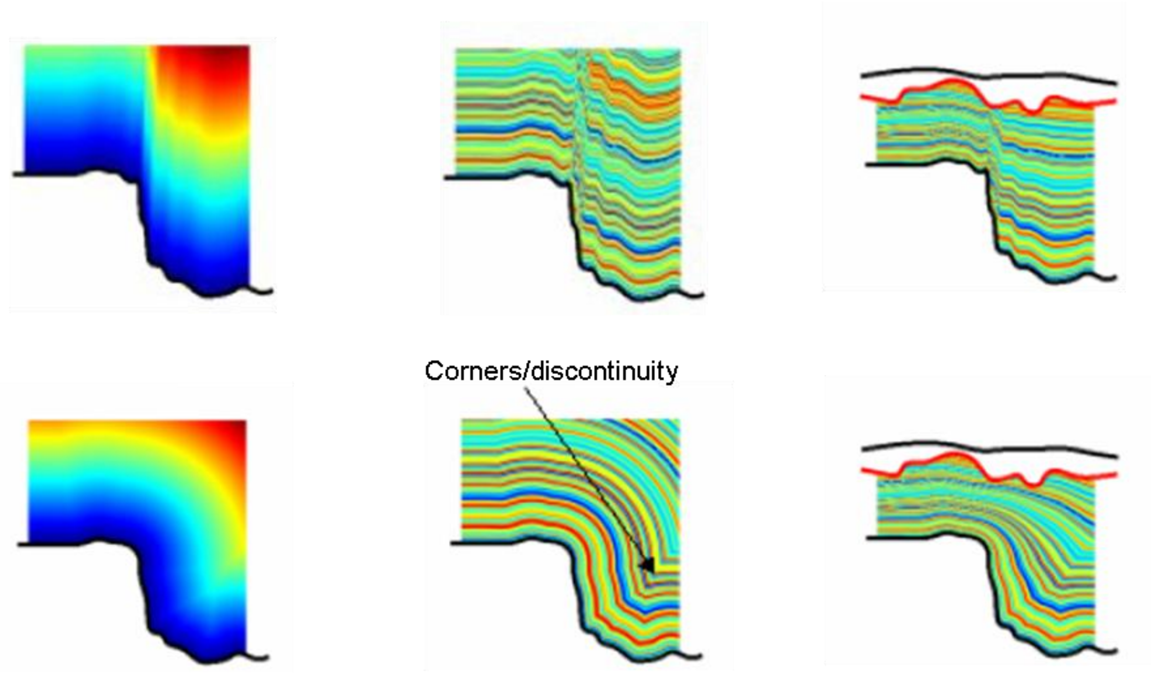

Figure 3.1: Similar deformation style on top, concentric deformation style at bottom. The left column shows distance field calculated in different ways, the second column shows corresponding property distribution, the last column shows an additional geometrical entity (red curve) which indicates an extra geological constrain is added to further delimit the property distribution. [Petersen et al., 2007].

A common practice to simulate seismic data in depth domain is to convolve a source wavelet with a reflectivity trace in vertical direction. The source wavelet has a signature that matches the one which is used in real seismic acquisition. Sheriff (2001) names a 1D convolution model, which is done by displaying those convolved 1D traces side-by-side and successively, a seismic image can be obtained. However, the 1D convolution model is based on the assumption that the earth is horizontally layered locally, therefore it only expresses for the vertical resolution of a migrated real seismic image and it does not account for the lateral resolution aspects of the migration process. Therefore, in order to correctly compare a simulated seismic image (synthetic seismic data) with a migrated seismic section obtained from industry (real seismic data) the synthetic seismic data have to be migrated as well. To be brief, aforementioned processes and relations can be expressed as [Toxopeus et al., 2008]:

Real prestack depth-migrated seismic image = *(3-1)*

Migration operator {Physical measurement {earth}}

$$\textit{Simulated prestack depth-migrated seismic image} = \underbrace{\textit{Migration operator}\ \{\textit{Forward operator}}_{\textit{Combined operator}}\ \{\textit{earth model}\}\} \tag{3-2}$$

Both migration and forward operation require a large amount of calculation, so that the computational costs of implementing a complete prestack depth-migrated seismic (PSDM) image that involves a migration algorithm following a forward operation is extremely high. In order to speed up PSDM process, a single operator produce the same result as that of combining migration and forward operator has been investigated for many years. For instance, a filtering result of a unit strength scattering point would be unit at the position of the scatter and zero elsewhere, in case of optimum migration operator. While in practice, because limitations of source (limited frequency spectrum) and acquisition geometry (limited recording aperture), the 'filtering result' will be slightly blurred.

Toxopeus (2006) names a spatial resolution filter to represent this combined operator, which is used to filter an earth model to generate the simulated migrated image. The spatial resolution filter is decomposed into a band-limit filter and an angle filter, of which the band-limit filter controls the frequency spectrum of wavelet, and the angle filter takes into account the incident angle with respect to extent of recording aperture. He also demonstrates the spatial resolution filter can be implemented by a product of these two filters in double-Fourier domain (expression 3-4). Details of description and derivation are referred to Toxopeus (2006) and Gerrit Toxopeus, et al. (2008).

$$\textit{Simulated prestack depth-migrated seismic image} = \underbrace{\textit{Band-limited filter}\ \{\textit{Angel filter}}_{\textit{Spatial resolution filter}}\ \{\textit{earth model}\}\} \tag{3-3}$$

$$\textit{Spatial resolution filter} = \textit{Band-limited filter} \times \textit{Angel filter} \tag{3-4}$$

The forward seismic simulation in Compound DDrx is carried out by applying this spatial resolution filter. Instead of forward modeling shot records and subsequently using a PSDM operator, an earth model is filtered by a spatial resolution filter, which can be easily obtained from a band-limited filter and an angle filter, to simulate PSDM data. The spatial resolution filter resembles the process of the physical measurements and the prestack depth-migration operation. The resultant simulated migrated data can be compared directly to the migrated real data.

Another advantage of implementing simulated migrated seismic by filtering an earth model with a spatial resolution filter is that our interested part within a model (e.g. a reservoir) can be decoupled from the earth model which is used to compute the spatial resolution function as long as overburden layers have little change [Gerrit Toxopeus et al., 2008]. It enables to quickly compute a forward seismic simulation of an adjusted reservoir without having to recalculate the spatial resolution filter, since band-limited filter and angle filter are only determined by characters of overburden and assigned recording characteristics like aperture and shot distance.

3.3 Finite difference modeling with the acoustic wave equation

The simulated migrated seismic as an operational module of Compound DDrx is only applicable for surface seismic, since receivers and sources are fixed on the surface. For forward VSP evaluation with diverse trial layouts included in chapter 6, we use a finite difference package which is developed by CREWES with Matlab. It uses the second order finite difference approximation for time derivative to solve acoustic wave equation in two dimensions. Receivers and sources can be positioned anywhere within the 2D medium (including on boundaries), and absorbing boundary conditions are implemented [Garry F. Margrave, 2003]. The following paragraphs briefly present basic mathematic formula used in this package to solve 2D wave equation by finite difference and summarize some items, with respect to numerical evaluation, should be carefully considered. More details about parameters in this package and its applications are referred to Garry F Margrave, 2003.

3.3.1 Mathematical formula

The classical scalar wave equation is:

$$\frac{\partial^2 \psi}{\partial t^2} = v^2 \nabla^2 \psi \tag{3-5}$$

where ψ represents the wave function, v is wave propagation speed, and ∇^2 is the Laplace operator that:

$$\nabla^2 = \partial_x^2 + \partial_y^2 + \partial_z^2 \tag{3-6}$$

Consider the above equation and Laplace operator in two dimensions:

$$\nabla^2 \psi(x,z,t) = \frac{1}{v^2(x,z)} \cdot \frac{\partial^2 \psi(x,z,t)}{\partial t^2} \tag{3-7}$$

$$\nabla^2 \psi(x,z,t) = \frac{\partial^2 \psi(x,z,t)}{\partial x^2} + \frac{\partial^2 \psi(x,z,t)}{\partial y^2} \tag{3-8}$$

Taking the second order approximation for the time derivative, which is:

$$\frac{\partial^2 \psi(x,z,t)}{\partial t^2} \approx \frac{[\psi(x,z,t+\Delta t) - 2\psi(x,z,t) + \psi(x,z,t-\Delta t)]}{\Delta t^2} \tag{3-9}$$

where Δt is the time step, into the 2D wave equation (3-7). The wave equation is changed to:

$$\nabla^2 \psi(x,z,t) \approx \frac{1}{v^2(x,z)} \cdot \frac{[\psi(x,z,t+\Delta t) - 2\psi(x,z,t) + \psi(x,z,t-\Delta t)]}{\Delta t^2} \tag{3-10}$$

Then the wavefield at $t+\Delta t$ can be calculated by the form:

$$\psi(x,z,t+\Delta t) \approx [2 + \Delta t^2 v^2(x,z) \nabla^2] \psi(x,z,t) - \psi(x,z,t-\Delta t) \tag{3-11}$$

This expression shows the estimation of wavefield at a future time $t+\Delta t$ requires knowledge of wavefield at actual time t and earlier time $t-\Delta t$.

The 2D Laplace operator ∇^2 is implemented by the second order finite difference approximation:

$$\nabla^2 \psi(x,z,t) \approx \frac{\psi(x+\Delta x,z,t) - 2\psi(x,z,t) + \psi(x-\Delta x,z,t)}{\Delta x^2} + \frac{\psi(x,z+\Delta z,t) - 2\psi(x,z,t) + \psi(x,z-\Delta z,t)}{\Delta z^2} \tag{3-12}$$

where Δx and Δz represent grid interval in two directions, and it is required that $\Delta x = \Delta z$. For higher accuracy, higher order approximations are needed at the expense of more computational time.

3.3.2 Parameters chosen

Though finite difference is a powerful and easily implemented method for solving partial differential equations, it can also bring extra artifacts and lead to unreliable result if parameters are not chosen properly. When applying finite difference to deal with wave equation problem, the parameters that need to be pre-defined can be divided into two categories. One is related with internal steps of algorithm, i.e., temporal steps and spatial steps; the other is relied on external requirement of desirable frequency and wavelength.

The following paragraph presents several relations among these parameters, which need to be satisfied in order to obtain an accurate result.

3.3.2.1 Relation between finite difference space and time step

Mitchell and Griffiths (1980) state the time stepping-forward method (3-11) is unstable in certain circumstances, which means the amplitude of the wavefield ψ will grow without bound as time step forward. Lines et al. (1999) derive the condition of stability for the time stepping-forward method, which is:

$$\frac{v\Delta t}{\Delta x} \le \frac{2}{\sqrt{a}} \tag{3-14}$$

where a is the sum of the absolute values of weights of wavefield terms in finite difference approximation for Laplace operator ∇^2. For the second order approximation (3-12), a = 8; while for the forth order approximation, a = 32/3. Also, velocity $v(x,z)$ is a function of x and z, therefore it suffices to use the maximum value in the model. Thus the stability conditions are:

$$\frac{v_{\max}\Delta t}{\Delta x} \le \begin{cases} \dfrac{1}{\sqrt{2}} & \text{second-order Laplacian,} \\ \sqrt{\dfrac{3}{8}} & \text{fourth-order Laplacian.} \end{cases} \tag{3.15}$$

As a result, the time and space sample rates can not be chosen independently, they should satisfy (3.15).

3.3.2.2 Aliasing

Aliasing refers to an effect/appearance that causes different signal to become indistinguishable when sampled, which due to insufficient samples. To avoid aliasing, signal should be sampled with sufficient samples according to Nyquist theorem both in time domain (frequency) and space domain (wavenumber):

$$f_{sampling} \ge 2 f_{\max} \tag{3.16}$$

$$n_{sampling} = \frac{1}{\Delta x_{sampling}} \ge \frac{2}{\lambda_{\min}} = \frac{2 f_{\max}}{v_{\min}} \tag{3.17}$$

where $f_{\max}$ is the maximum frequency in original signal, $n_{sampling}$ is the sampling spatial frequency (wavenumber), $\Delta x_{sampling}$ is spatial sampling rate, $\lambda_{\min}$ *is the minimum wave length in signal,* $v_{\min}$ is the minimum velocity in the model.

One should be aware that the spatial sampling rate $\Delta x_{sampling}$ is different from finite difference space sample rate Δx, and temporal sampling rate $\Delta t_{sampling}$ $(=1/f_{sampling})$ is not equal to finite difference time sample rate Δt.

3.3.2.3 Grid dispersion

The earth model has to be divided into many cells to implement finite difference. If the size of cells approximate to the wavelength of signal, waves disperse with increasing travel-time, which means signal with higher frequency travel slower than signal with lower frequency and, consequently, substantial tailing arises with increasing traveltime. This phenomenon is known as grid dispersion [Kelly et al., 1976].

Grid dispersion can be avoided by taking more samples than the Nyquist criterion of two per wavelength. A good rule of thumb is about five to ten samples per wavelength.

$$\Delta x = \frac{\lambda_{\min}}{5 \sim 10} = \frac{v_{\min}}{(5 \sim 10) f_{\max}} \tag{3.18}$$

Typically, in a creation of model, the desired temporal frequency and minimum velocity are known. Then, the finite difference space step Δx can be chosen according to expression 3.18. After that, the finite difference time step Δt is chosen according to expression 3.15 to achieve stability.

Chapter 4

Model construction

This chapter deals with construction of a realistic 2D model based on the seismic cross section (Figure 2.7) selected in NW pool. The primary part is to reconstruct architectures of point bar deposits that dominate the local depositional processes in McMurray. Based on logging data, we create an innovative method to represent inclined heterolithic stratification (IHS) sequence of a point bar system, which is the major structure of laterally accretional point bar deposits in meandering fluvial environment. After the model is ready, surface seismic simulation is made and compared with real seismic data in order to 1) evaluate the validity of our model; 2) specify point bar seismic responses. Meanwhile, the validity of constructed is also evaluated by comparing synthetic and actual logging data.

4.1 Architecture of Point bar deposits

In chapter 2, it has been stated that tidally influenced meandering fluvial point bar dominate the middle McMurray deposits, where the main bitumen resource located. In order to construct internal architecture of this lateral migration point bar system, we need to investigate what main features of meandering channel point bar deposits are and how they are formed during deposition.

As meander belts migrate, flow incises along the cut bank on the outside of a bend and deposits a point bar along the inner part of the bend. While when river flow encounters with resistant sediments, e.g. resistant valley side bedrock and mudstone filled channel or oxbow, lateral freedom is restricted and the meander have to adjust migration course to accommodate the obstacle with resultant merging scroll bars against resistant sediment (Derald G. Smith at el., 2009). As a result, point bar deposit exhibits convex-shaped scroll bar morphologies, whereas counter point bars are preserved as concave-shaped scroll patterns (shown in Figure 4.1). And these two types of scrolls contact at meander channel inflection or crossover point, i.e., the point where scroll curvature change sign.

Both point bar and counter point bar deposits present inclined heterolithic strata (IHS) sequences and IHS normally are represented by interbedded siltstone and sandstone layers which indicate sedimentation under influence of variable currents. For those interbedded units of IHS in the McMurray formation, Thomas et al. (1987) state they potentially represent seasonal fluctuation in channel discharge, and Smith (1988) adds they are widely considered to be tidally modified, formed in an estuarine setting. Due to the energy of the tidal current varies cyclically, thus its capacity to carry sediments varies in the same manner. At the highest tides (spring tide) the current is strongest, and it enables more transport and deposition of sand. When it comes to neap tide, the current with less energy will transport reduced bedload or there may be no sediment at all. The gravitational variation in neap spring cycle leads to cyclic variation of current energy, which sequentially carries different load, finally deposits in a same place with cyclic variation deposition. Figure 4.2 is a conceptual model showing possible appearance of IHS in point bar deposits, both in dip-section view and plan view.

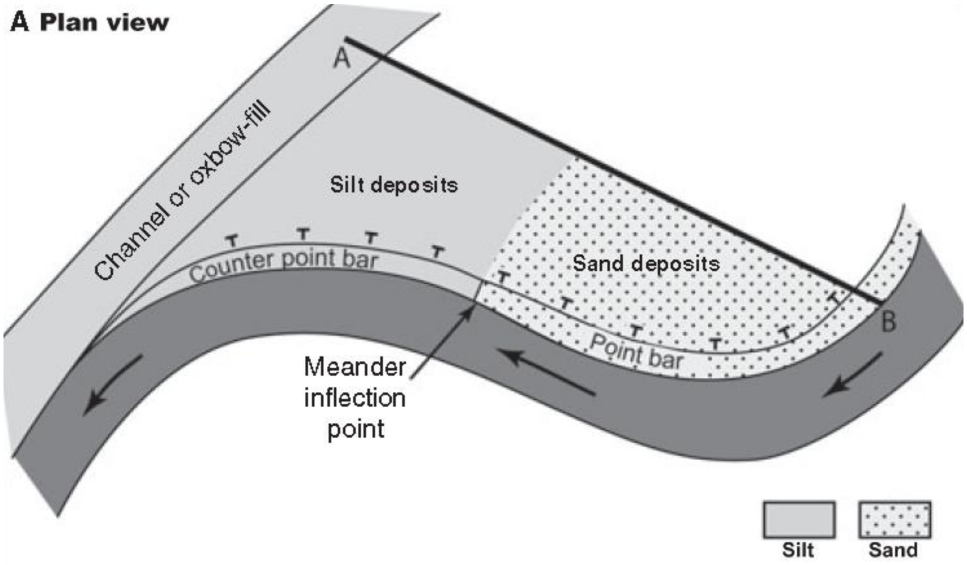

Figure 4.1: Schematic diagram shows how point bar and counter point bar develop in a meandering belt system. [Derald G. Smith, 2009]

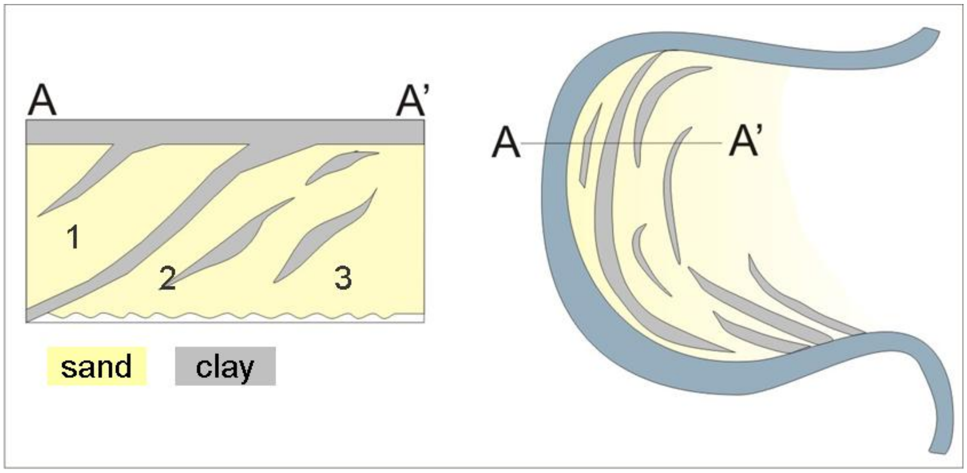

Figure 4.2: Conceptual model illustrates IHS set within point bar deposit, also shows basic types of fine member down-dip continuity viz.: 1) discontinuous, up-dip attached; 2) continuous; 3) discontinuous, irregular. Notice that this model only accounts for very simple variability between sand and shale, which is not full suite of IHS faces. [Thomas et al., 1987]

4.2 Point bar system representation

Reconstructing architectures of point bar deposits is the core of our model building. We separate the construction into two stages: 1) based on specific logging data, we create a local/vicinal point bar deposits with lateral extension relied on the thickness of the point bar and dipping angle of IHS (Figure 4.6); 2) extend the structure of local point bar deposits to a wider coverage point bar of interest (global point bar deposits).

4.2.1 Creating local point bar deposits

4.2.1.1 Property function and distance field

In chapter 2, it has been described that a formation (a spatial property distribution) is created by combing assigned geometrical entities with property entities (property functions) by means of distance field. This formation can be further delimited or/and ordered (stacked with other formations) in terms of logical entities. Therefore, when we consider building a solitary point bar deposit, we first need to find out what should be chosen as geometrical entities, how an assigned property function looks like and how to decide distance field.

For a simple formation (shown in Figure 4.3) , a distance filed is implicitly indicated as target points' distance, in the direction of a property function defined away from origo of the property function which meanwhile moves along the geometrical entity. The defined direction can be fixed relative to the background, or relative to the geometry itself, e.g. normal direction of a curve or surface. Although the direction could be a mixture of these two, that is beyond the scope of this study. As soon as the direction is defined, we can always find out that properties do not change along curves that are paralleling, either in the sense of concentric or similar deformation, to the geometrical entities. If we define the curve (geometrical entity) along which properties do not change as one dimension and the direction along which property function defined as another dimension, to a certain extent, we will be able to state that a 2D spatial property distribution problem can be expressed by a single 1D property function in a reference coordinate system, in which the property only varies in one dimension.

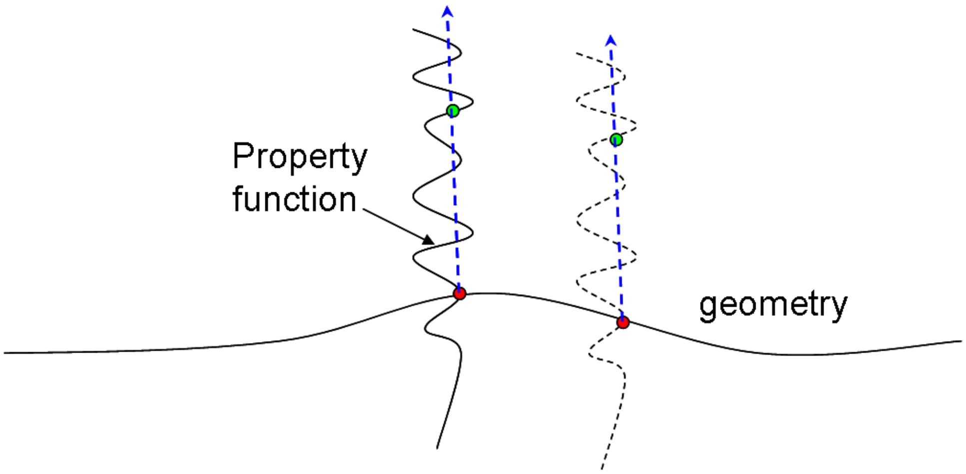

Figure 4.3 Schematic diagram shows how property distribution is implemented for a simple formation. The red dot represents the origo of property function, the green dot represents a target point within the formation, and the blue dash line implicitly indicates the distance filed which includes distance (in one dimension) between target point and origo and direction along which property function defined. As the origo moves along the geometry (the other dimension), the green dot follows a paralleling path.

While for a point bar construction (shown in Figure 4.4), inclined units are assigned as geometrical entities (one dimension), and property functions (one dimension) are defined along inclined units also, i.e. two dimensions totally overlap. Thus in order to implement 2D spatial property distribution, we need to define another function that explicitly extends properties to another dimension different from inclined units, here we set the dimension along the direction of developing point bar. Specifically speaking, given point bar deposition is the interference of gravity and current variation, the defined property function indicates the influence of gravity, while the other function implies how current energy varies during deposition, which is reflected by alternation of water level, flow velocity and etc.

4.2.1.2 Deriving property and variation function based on logging data

Decompose logging data

Figure 4.5 shows a segment of gamma ray from well 0221, the depth range corresponds to the upper point bar deposit at that position. The log values in this segment can be decomposed into two parts: one represents a general trend from top to bottom, which can be obtained by linear curve fitting and is named as borehole property function (BPF); the other indicates differences between true values and BPF, which can be easily obtained by

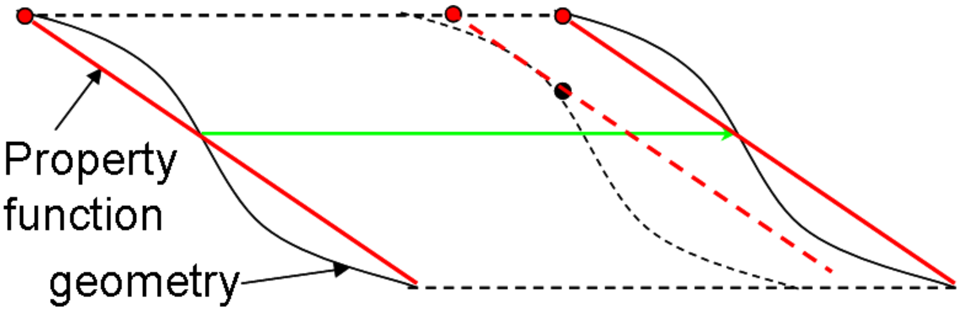

Figure 4.4: Schematic diagram showing how property distribution implemented for a point bar formation. The red dot represents origo of assigned property function and the black dot represents target point in space. In order to reach that point, we need another function to 'guide' property function to 'get' there. The green line represents the new defined function. Please note that the green line can be any shape as long as it indicates variations of current energy during deposition.

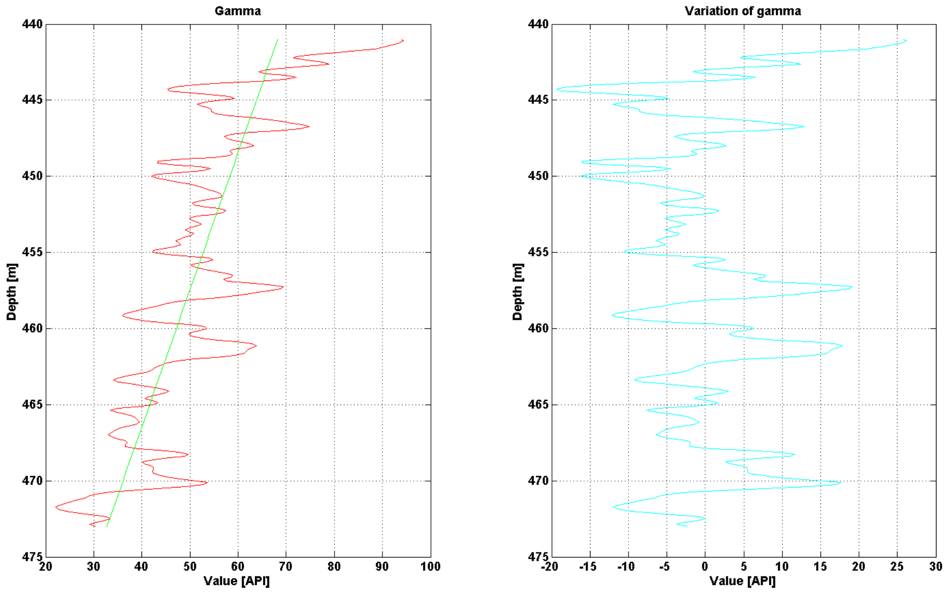

Figure 4.5: Illustration of decomposing logging data into BPF and BVF. The red curve indicates a segment of gamma ray within point bar deposits in well 0221, the green line indicates the general trend of logging data, which is named BPF, and the cyan curve represents BVF which obtained by subtracting values of the green line from the red curve.

subtracting BPF value from logging data at the same depth and is called borehole variation function (BVF).

From borehole to inclined (heterolithic) strata

As discussed in 4.2.1.1, in order to build a point bar deposit, we need to know the property function along inclined units which we name as IPF and another function which indicates variation of current energy and is named as variation function along inclined units (IVF). Figure 4.6 illustrates simplified relations among BPF, IPF, BVF, IVF and logging data. Shown in the upper diagram, the schematic log on the right side represents a BPF, which is recorded along the well. In parallel with this, our desired IPF can be understood as a log recorded along an inclined unit (the dipping solid black line). Considering geometry relation between vertical well and dipping units, the IPF can be obtained by partially scaling BPF, i.e. scaling well depth to length of inclined unit.

The diagram at the bottom demonstrates relation between BVF and IVF and influence of IVF on property distribution in point bar deposits which could result in architecture of IHS. Three points need to be noticed when deriving IVF from BVF. Firstly, we should be aware that the length of IVF (the pink dash line) and the effective length of IHS (segment between upper and lower boundary) are not equal. However, due to the dip of IHS normally is very small, it is reasonable to approximate the effective length of IHS as the length of IVF. Secondly, depth of BVF should be scaled to length of IVF. Last but not least, the magnitude of IVF and magnitude of BVF should be scaled by the ratio of IHS length to well depth, and these magnitudes indicate how IPF moves long IHS and BPF move along vertical direction respectively, including directions and distances. Figure 4.7 demonstrates relation between BPF and BVF, IPF and IVF, and indicates the geometrical cornerstone of construction point bar deposits by logging data.

Take sigmoid shape into account

Sigmoid shape is the best known representative for inclined units viewed in true-dip sections**.** We assign our property function (IPF) to corresponding geometrical entity (sigmoid curve). Given IPF is a linear function in terms of length, property varies linearly along the sigmoid curve, i.e., path gradient of property function along sigmoid is constant:

$$\frac{df}{dl} = c \qquad (5\text{-}1)$$

where f is property function, l is arc-length of sigmoid curve. (5-1) indicates property' variation with length is equally distributed along sigmoid curve.

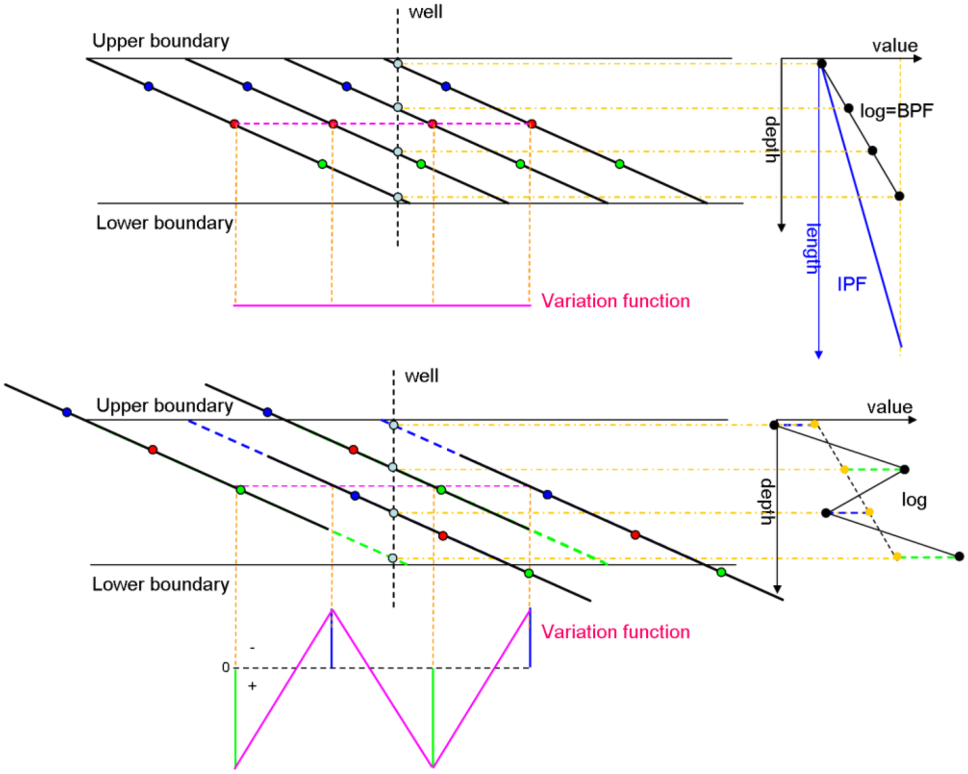

Figure 4.6: Schematic diagrams illustrate relation between BPF and IPF and relation between BVF and IVF. The dipping solid black lines represent inclined units. Blue, red and green dots indicate different positions at IPF. The upper diagram demonstrates a way to derive IPF from BPF by replacing well depth with length of inclined unit while keeping property values. The lower diagram exhibits influence of IVF on property distribution of the conceptual point bar deposits which results in architectures of IHS. The black zigzag on the right side indicates a log which is recorded along the vertical well, and the pink zigzag at the bottom represents IVF, whose values stand for distances that IPFs should move up and down along their assigned inclined units in order to obtain the log on the right side.

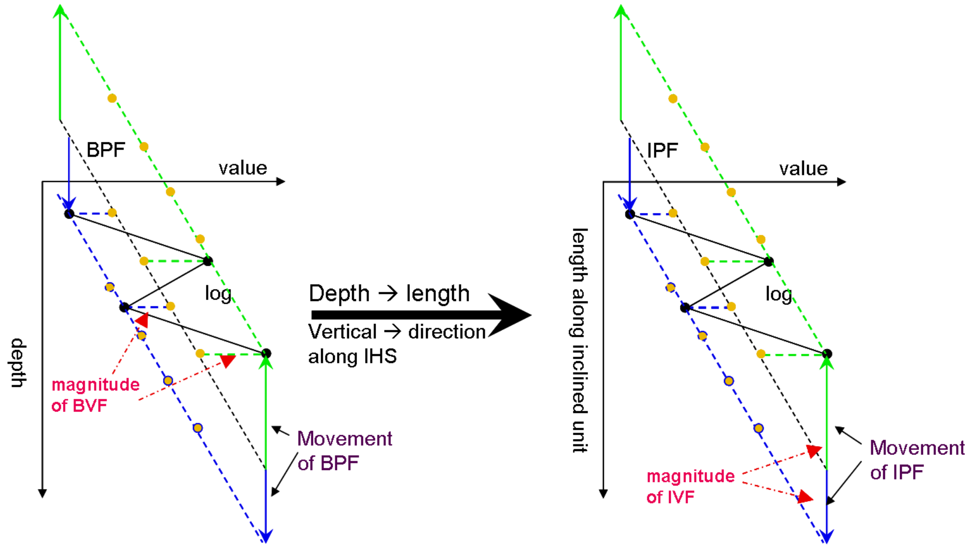

Figure 4.7: Schematic diagrams illustrate relation between BVF and BPF, IVF and IPF, and the way of their combination that contribute to log data. The diagram to the left, demonstrates borehole log can be decomposed to BPF and BVF. Values of BVF equal to differences between log values and BPF. At a certain position, e.g. the well position, movements of BPF along well direction lead to the oscillation of logging data around BPF values which comprise BVF, and these movements correspond to fluctuation of deposition environment. Given a linearly BPF increasing with depth, a positive magnitude of BVF (green short dash line) at a certain position indicates that a larger property corresponding to a relative deeper position at BPF is required at this certain position, and the depth difference (solid green line with an arrow) is calculated from the value of BVF at this certain position and the slope of BPF. The diagram to the right demonstrates, instead of BPF and BIF, how IPF and IVF are related with logging data. Both of them can be converted from left diagram by applying a scaling factor on depth to extend them to length of inclined units and transferring movements of BPF along vertical direction to movements of IPF along inclined units. It should be noticed that magnitudes of IVF directly equal to movements of IPF, while magnitudes of BVF equal to value differences between logging data and BPF.

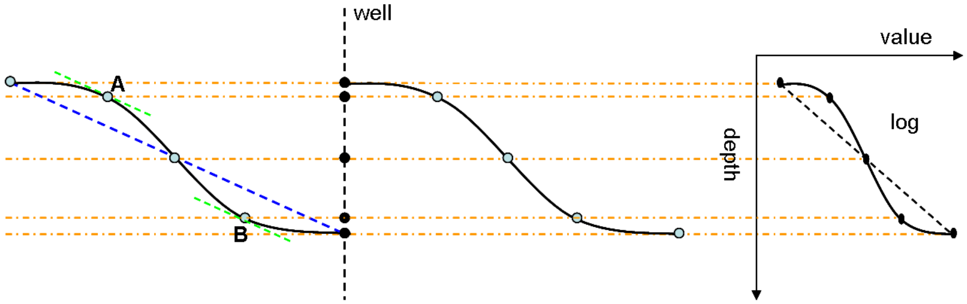

Figure 4.8: A schematic diagram shows the influence of sigmoid shape on property distributions, given linear BPF and IPF. Sigmoid curves represent IHS, blue dash line connect two ends of a sigmoid curve, green dash lines are tangents of the curve at two marked points with the same slope as the blue dash line.

Shown in Figure 4.8, a well is drilled vertically, and the logging data (vertical property variation) could be understood as property variation along sigmoid curve projected laterally to a vertical line. Considering difference between a sigmoid curve and a vertical line, the behavior of property distribution along the well is different from property distribution along the sigmoid curve, i.e., property of distal part of the well varies more significantly than that of central part does (the black squeezed sigmoid curve shown in the graph to the right side of Figure 4.8). Seen from last section, a log data can be decomposed into a BPF, which indicates general varying trend of property, and a BVF, which represents vertical movements of BPF. In Figure 4.8, we assume there is no vertical movement of BPF during point bar deposition, i.e., BIF = 0 in this case. Thus, the resultant log data only consist of BPF, i.e. log = BPF, which is not a straight line. While the way to construct architectures of point bar deposits we described above is based on the BPF is a linear function, otherwise it will be difficult to figure out an explicit relation between vertical movements of BPF and values of BVF, which is no longer linear if BPF is a non-linear function.

Therefore, in order to construct architectures of point bar deposits with sigmoid geometry, some adjustments are needed. Now, we can split a well log to three parts:

$$log = Combination(BPF, BVF, adjustment)$$

This indicates a log is an interference of BPF, BVF and adjustment, and the *adjustment* can be made either to *BPF* or *BVF*. Since we want to keep the linearity of BPF, the following paragraphs mainly focus on how to modify BVF while the method to modify BPF (or IPF) is briefly discussed in Appendix A.

Our goal is to make the sigmoid-shape log approach the straight black dash line. A function f represents sigmoid curve of inclined unit, and k is absolute value of the slope of blue dash line. It is defined properties[1] will be compressed (i.e. properties' variation with length will increase) after being projected if these properties are situated at points where the first derivative (f') follows: $|f'| < k$; while properties[1] will be stretched (i.e. properties' variation with length will decrease) after being projected if these properties are located at points where $|f'| > k$. Shown in Figure 4.8, two points (A and B) on the sigmoid curve with short green dash lines indicate two points at which $f'=k$. Properties[1] projected from points located outside AB are compressed by a factor of $|f'|/k$ (<1), while those projected from points located inside AB are stretched by a factor of $|f'|/k$ (>1). It is these compressing and stretching that leads to shape of the well log deviates from the straight line and forms the squeezed sigmoid shape. In order to compensate these deviations and without losing the linearity of BPF, we scale space steps of discretized BVF by factors of $k/|f'|$, where f' are discretized first derivatives of BVF.

Since IVF relates with BVF linearly, as soon as BVF is obtained, IVF can be easily derived by scaling values and depth of BVF with ratios discussed at the beginning of this section. Figure 4.9 indicates scaling and compensating factors based on the given sigmoid curve. It is interesting to notice that modifying factors (for compensation) have much larger influence on the sample steps situated in distal parts of BVF than in central part, and this explains why only central part of IVF is used to reconstruct point bar deposits.

4.2.1.3 From local variation function to global variation function

Due to lateral extent of a local point bar structure is constrained by its thickness and dip of inclined units, in order to build a large point bar deposits, we shall extend local property distribution laterally. Sigmoid shape and IPF are relative easy to obtained by observing seismic section and analyzing logging data, thus creating a global IVF covering the whole area of interest is the key for this implementation.

The following paragraph presents a way to construct an IVF with larger coverage by re-producing several elementary IVFs from derived local IVF and then connecting them together, given depositional environment of the whole large area of interest is similar to that of the local point bar deposits. Figure 4.10 shows a process chart including all phases from input (a derived local IVF also called Arcmod function) to final output (a predicted

---

[1] Property here indicates the property point and its distance to next property point.

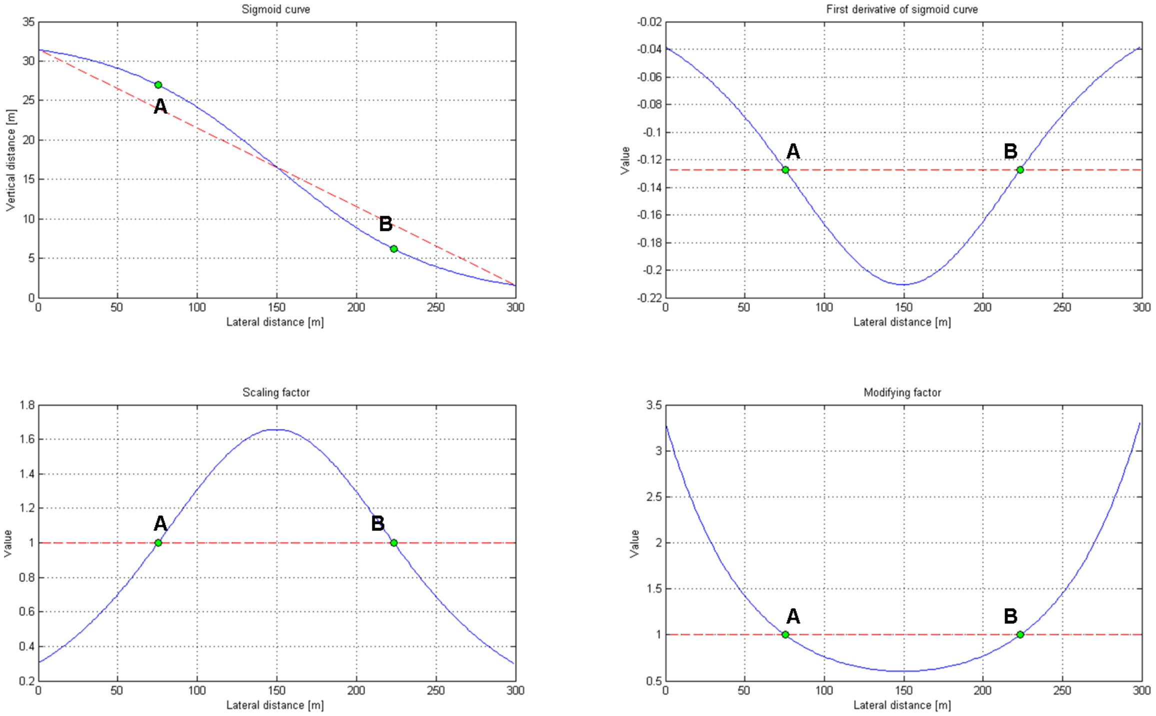

Figure 4.9: The sigmoid curve used to construct point bar deposits. The upper left is the sigmoid curve with a dash line connecting two ends, A and B indicate two points on the curve at which the first derivative is equal to the slope of the dash line; the upper right is the first derivative of the sigmoid curve, while the red dash line indicates the slope of the straight on the left side; the lower left represents the scaling factor, |*f'*|/*k*, that are enforced on properties when projected to the well; the lower right represents the modifying factor, *k*/|*f'*|, which is the inverse of scaling factor to compensate the effect of scaling factor on properties' distribution.

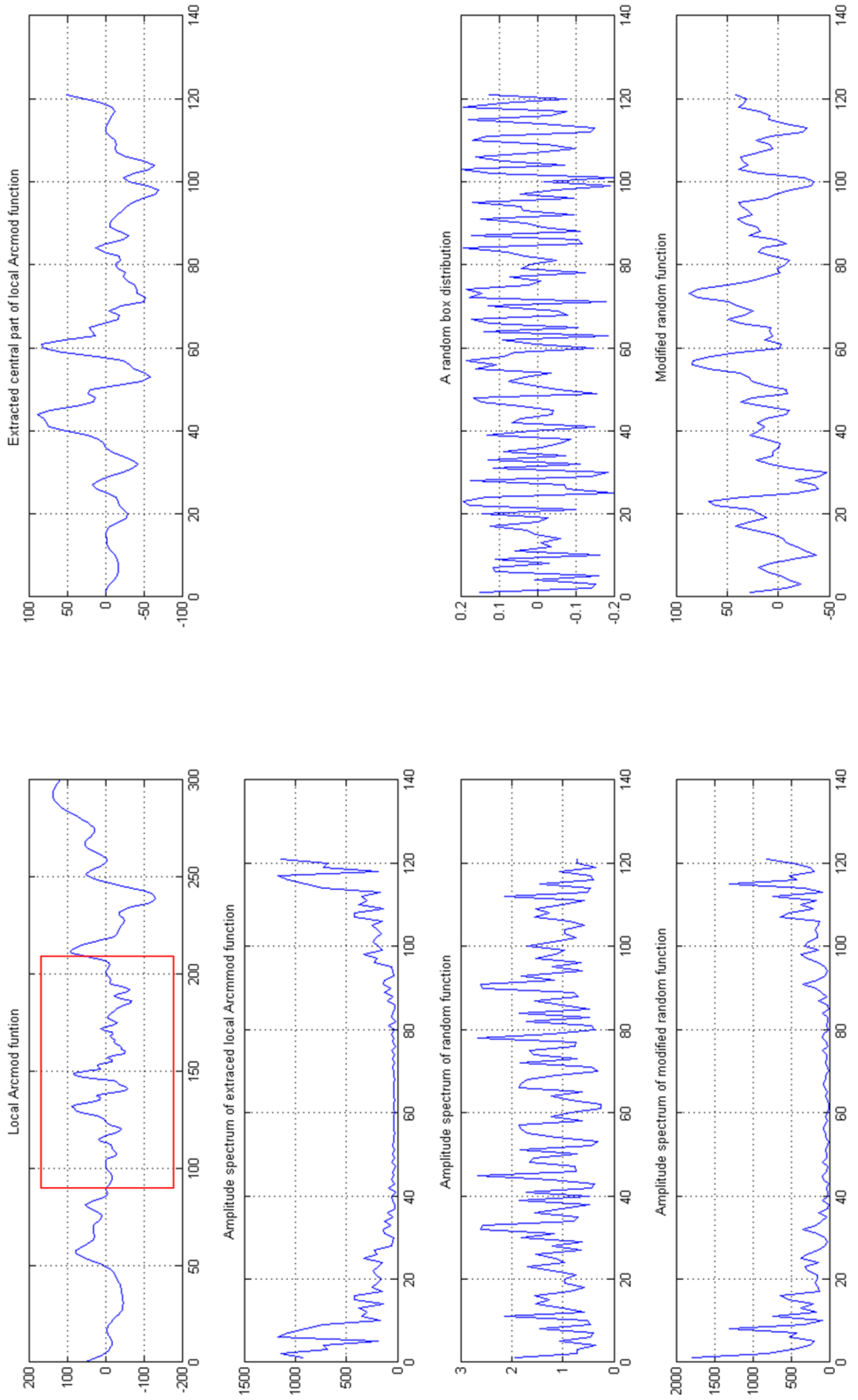

Figure 4.10: A procedure chart for creating elementary IVF from known local IVF. The red box indicates extracted part to produce elementary IVF.

elementary IVF, also called modified random function). First, due to the reason, mentioned in the end of last section, that sample steps at distal parts of IVF is highly affected by modifying factor, they will be not reliable for point bar structure construction, we only extract the central part of local IVF as effective IVF to produce our elementary IVFs. In order to preserve characteristics of extracted part of local IVF as many as possible, its energy spectrum is calculated which is shown in the second row. Then we take a random function with box distribution and set its length equal to the length of extracted IVF, then apply Fourier transform on it to calculate its amplitude spectrum. After this, the amplitude spectrum of random function multiplies with the energy spectrum of extracted IVF in order to extract/create characteristic of effective IVF from the random function. In the end, we apply inverse Fourier transform on the product, we achieve a modified random function with the similar amplitude and frequency characteristics as extracted IVF. In the same way, we can create as many modified random function (elementary IVF) as we want and keep them mutually different by setting different 'seed' when create random functions. One should be aware that sample steps of the IVF we obtained from last section are modified by modifying factor thus are different, in order to apply Fourier transform on the extracted part, the IVF should be resampled by equalized sample steps in advance.

In order to avoid sharp jumps at contacting point, each elementary IVF is applied a 4-point amplitude shaping filter and located with 10 samples overlapped on each side when connecting with others (Figure 4.11).

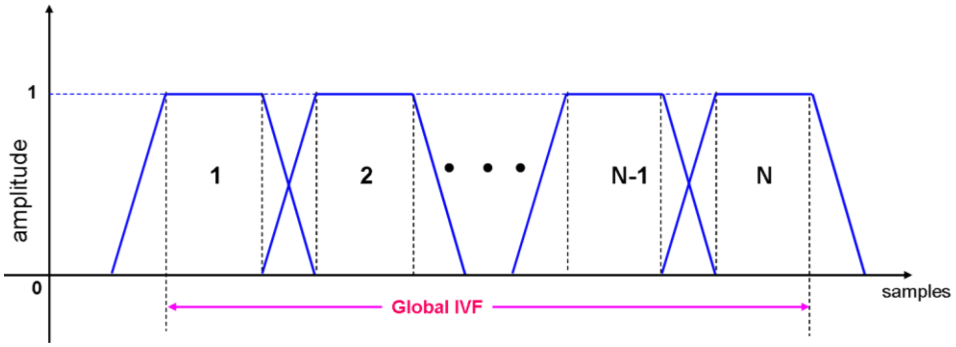

Figure 4.11: Schematic diagraph shows how elementary IVFs are connected to form a global IVF.

4.3 Model building

Now we are ready to start model building based on the seismic section and logs from controlling wells. Figure 4.12 shows the cross section with indication of projected positions of controlling wells, in which numerous horizons of geologic significance can be picked and point bar's inclined features present pronouncedly in McMurray.

4.3.1 Point bar deposit model

Analyzing extracted logging data in McMurray: high correlation between gamma and density logs indicate density is a good lithology indicator (Figure 4.13), properties' relation of different wells shown as clusters in Figure 4.14 implies similar depositional environment. In Figure 4.13, a recognizable sharp jump in gamma indicates an erosive surface subdividing point bar deposits in McMurray into two separate stages with fining-up features in both segments, which enable us to build two stacked point bar architectures separately.

Based on the similarity of depositional environment, it is reasonable to predict property distribution by extrapolating local point bar deposits. Considering the distance between true position and projected position of a well and its relative position in the seismic section, we select well 0221 and 1415 to derive local and global property function respectively, and then choose the average of two created global IVF as the final IVF for constructing architectures of point bar deposits of interest.

After creating point bar model with straight top and bottom boundaries, we need to map those straight boundaries to corresponding horizons picked in seismic. While mapping simply implies followed tectonic and/or geological events affect the preceding deposits. It also should be noticed that the lower point bar is partially overlapped by the underlaid Devonian top in the model, which seems to be against the chronology of geological events. This 'geologically reversed' implementation is because the Devonian top has such significant topography features that highly influence local depositional process on it, which results in an effect as succeeding deformation and/or erosion.

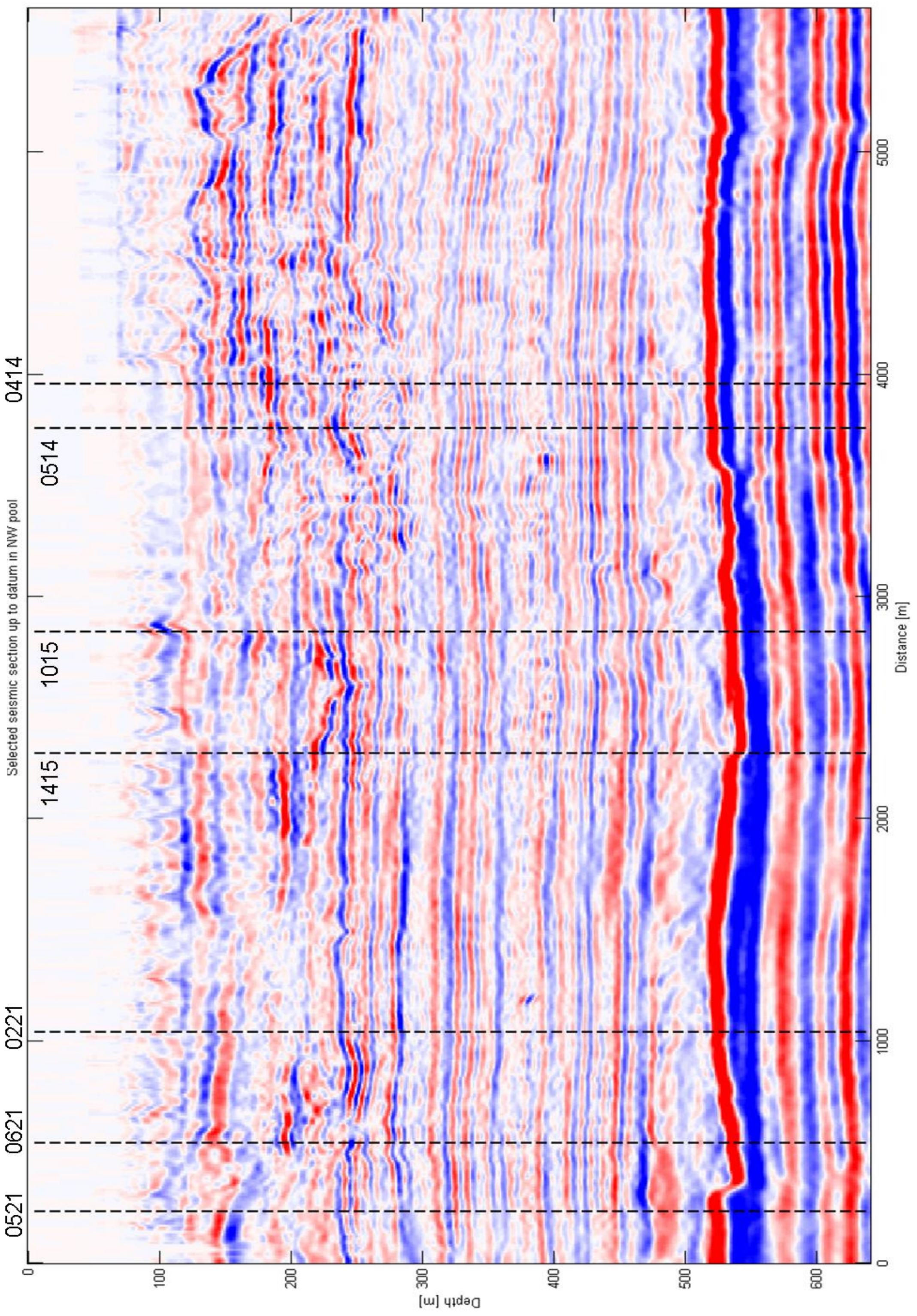

Figure 4.12: Seismic section with indication of projected positions of controlling wells.

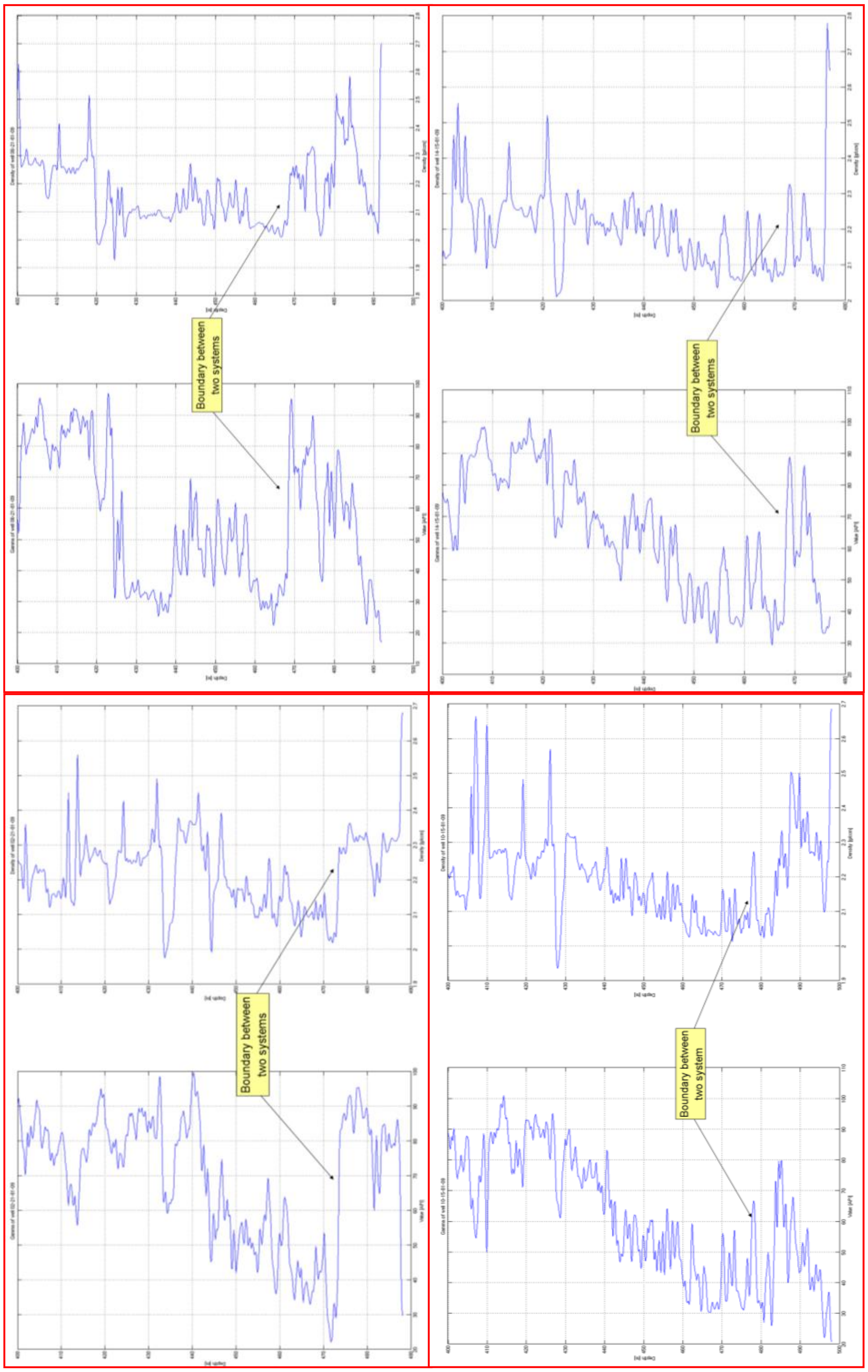

Figure 4.13: Four sets (well 0221, 0621, 1415 and 1015, in clockwise direction) of gamma ray and density logs within McMurray formation, all of which present fining-up features of point bar deposits and high correlation between density and gamma ray, which implies density is a good lithology indicator. Big jump at lower McMurray indicated by black arrows is proposed to be the boundary between two point bar deposits.

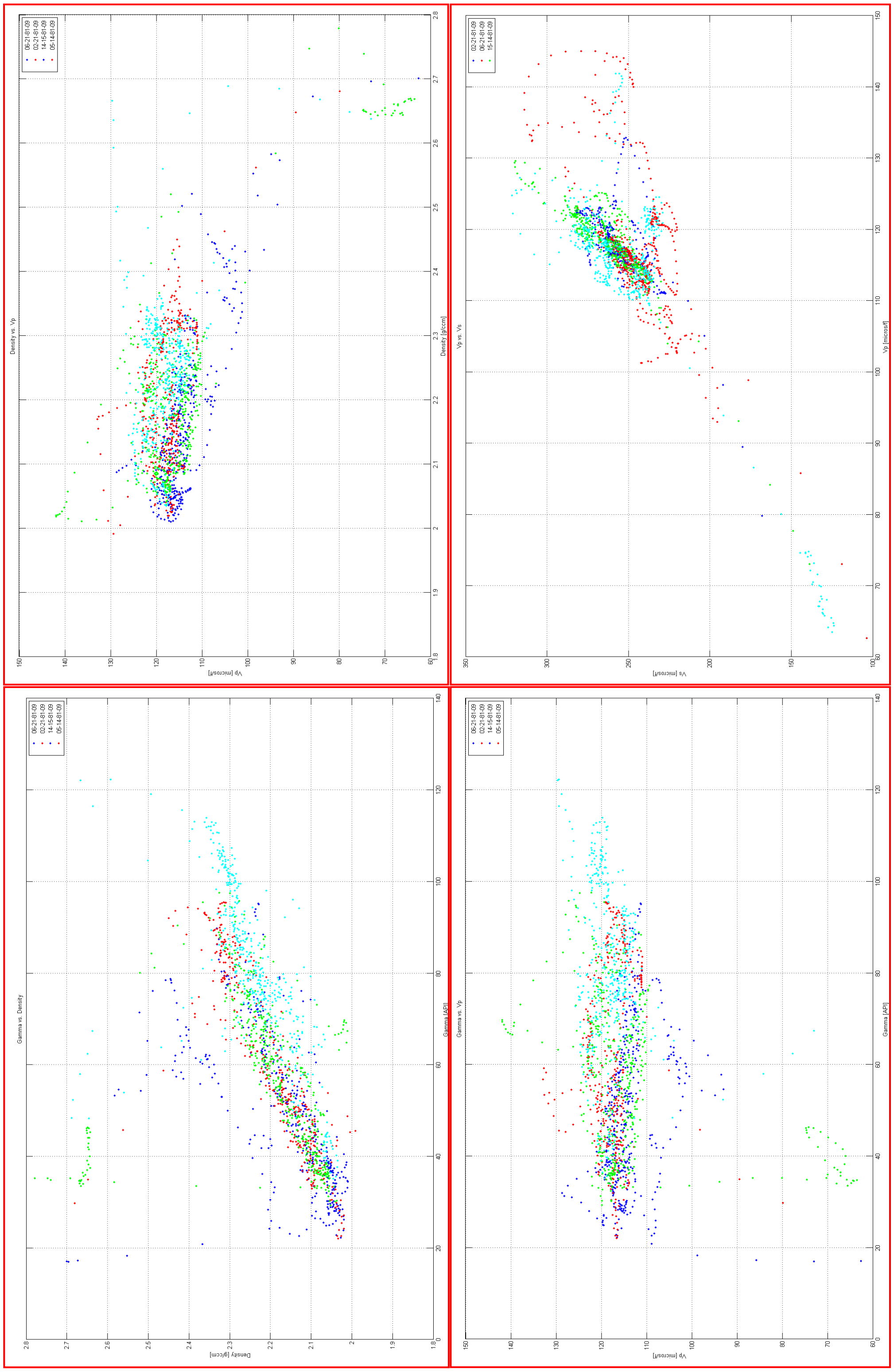

Figure 4.14: Cross-plot of different properties with four selected wells indicated by different colors. Four plots, in clockwise direction, are density vs. gamma, density vs. Vp, Vp vs. Vs and gamma vs. Vp.

4.3.2 Overburden and final model

Compared with point bar deposit construction, creation of overburden of almost flat layers is relatively straightforward. It required carefully picking horizons in seismic and then aligning them with interpreted formation tops from logging data. As seen in Figure 4.12, there are seven controlling wells near the cross section, dash blacked lines indicate their projected positions, in order to align horizons picked in the seismic section with formation tops of wells, we extract seven cross sections each of which goes through a true and projected position of well (See Appendix Figures).

Besides overburden model and point bar model, an abandonment channel is also delimited in seismic section and created separately. After these sub-models are in place, we combine them in a chronological order to create the final model (Figure 4.16).

4.4 Seismic simulation and model validity evaluation

4.4.1 Seismic simulation

Seismic simulation helps to relate geological settings with seismic responses. Comparing synthetic data with real data, in one hand, assists to recognized meaningful features in real section; in the other hand, provides information to evaluate validity of constructed models. Surface seismic simulation toolkits are involved in the model builder -- Compound DDrx, we operate Toxopeus-forward simulation on the created model, of which results are simulated migrated seismic that can be directly compared with real data.

Before starting simulation, there are several parameters to be set, of which wavelet-related parameters are the most important, including frequency range, central frequency, phase rotation and time shift. In order to obtain data that matches well with real data, these parameters should be set carefully.

In the real data (Figure 4.12), there are two pronounced horizons near Devonian Top at which a sharp impedance contrast exist. Thus minimum phase wavelet should be selected to carry out the simulation, while minimum phase wavelet can be obtained by applying a -90 degree rotation on zero phase Mexican hat function which is the default wavelet. After phase rotation being fixed, the time shift, central frequency and frequency range

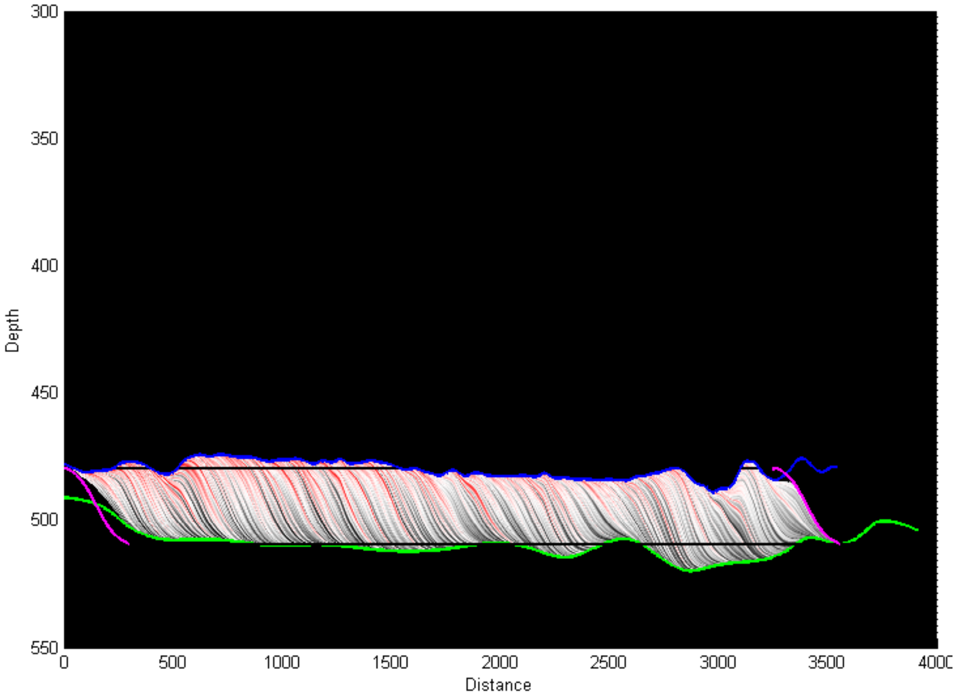

Figure 4.15: Deformed point bar deposits

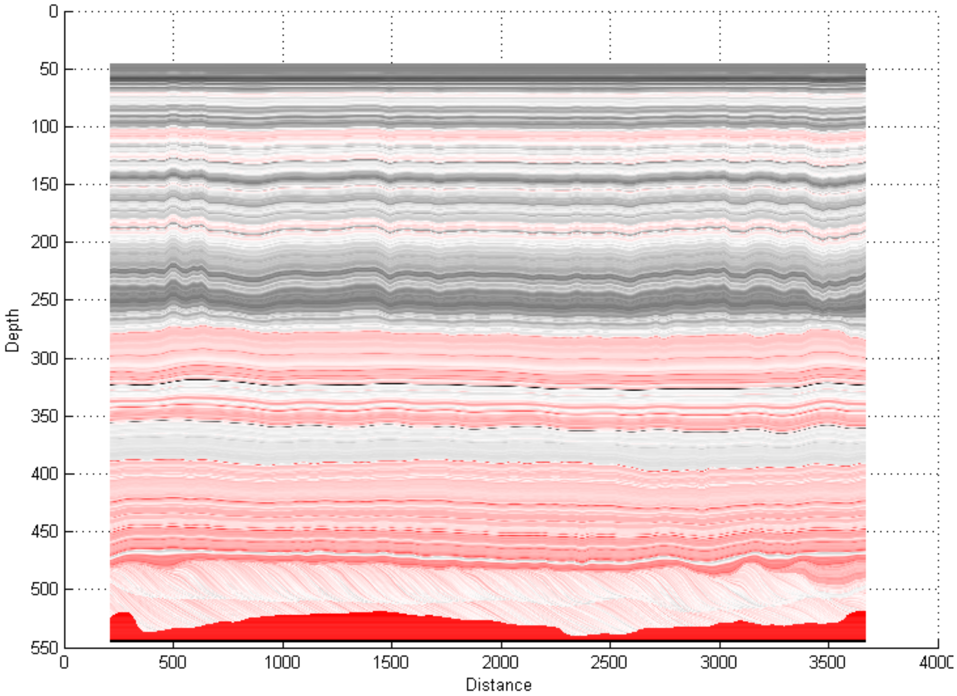

Figure 4.16: Density model section

can be figured out through several trial simulations. Figure 4.17 is resultant simulated migrated seismic.

4.4.2 Evaluation of model validity

Comparing real seismic section (Figure 4.12) with synthetic simulated migrated seismic (Figure 4.17), the following observations can be achieved:

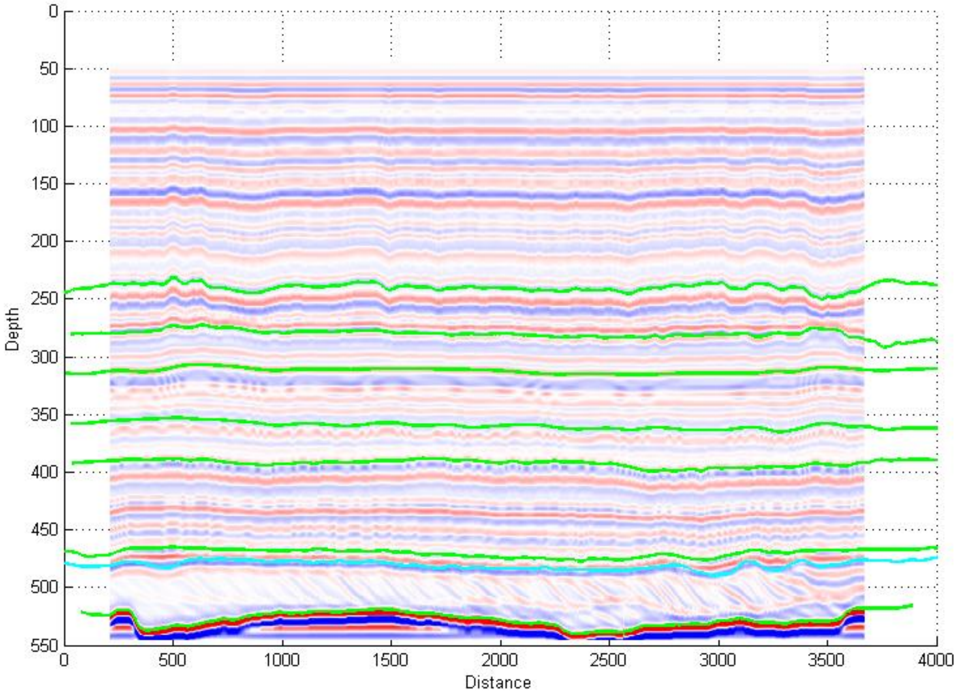

Figure 4.17: Synthetic seismic section

a) Most horizons of overburden match well with real data. Horizons situated between McMurray Thief Zone Top and Grand Rapids PORO SS Base are highly consistent across the whole section, except relative high frequency showing near Grand Rapids PORO SS Top in real data.
b) Due to poor continuity of horizons between Grand Rapids PORO SS Top and Grand Rapids PORO SS Base shown in real data, it is difficult to reconstruct those seismic features based on a layered overburden model.
c) For point bar deposits, seismic features of IHS are very pronounced in synthetic section, lateral alternations of high amplitude (red color) and low amplitude (black color) indicate interbedded sandstone and mudstone result from fluctuation

of water levels during point bar lateral accretion. The boundary between two point bar deposits can be easily recognized in synthetic section and its corresponding seismic response in actual data are those high amplitude spots near Devonian Top that relate with clay-based deposits in the lower point bar.

Besides seismic assessment, comparing synthetic logging data with actual logs is a more direct way to evaluate validity, since synthetic logging data (i.e. property distribution) can be directly extracted from model itself. But one should be aware that logging comparison is only valid at or near places where wells are available. Figure 4.18 shows comparison of density and gamma from well 0221 and 1415. All of the four sets present a very good consistence between synthetic data and real data, with respect to events positions, general trend, frequency and amplitudes.

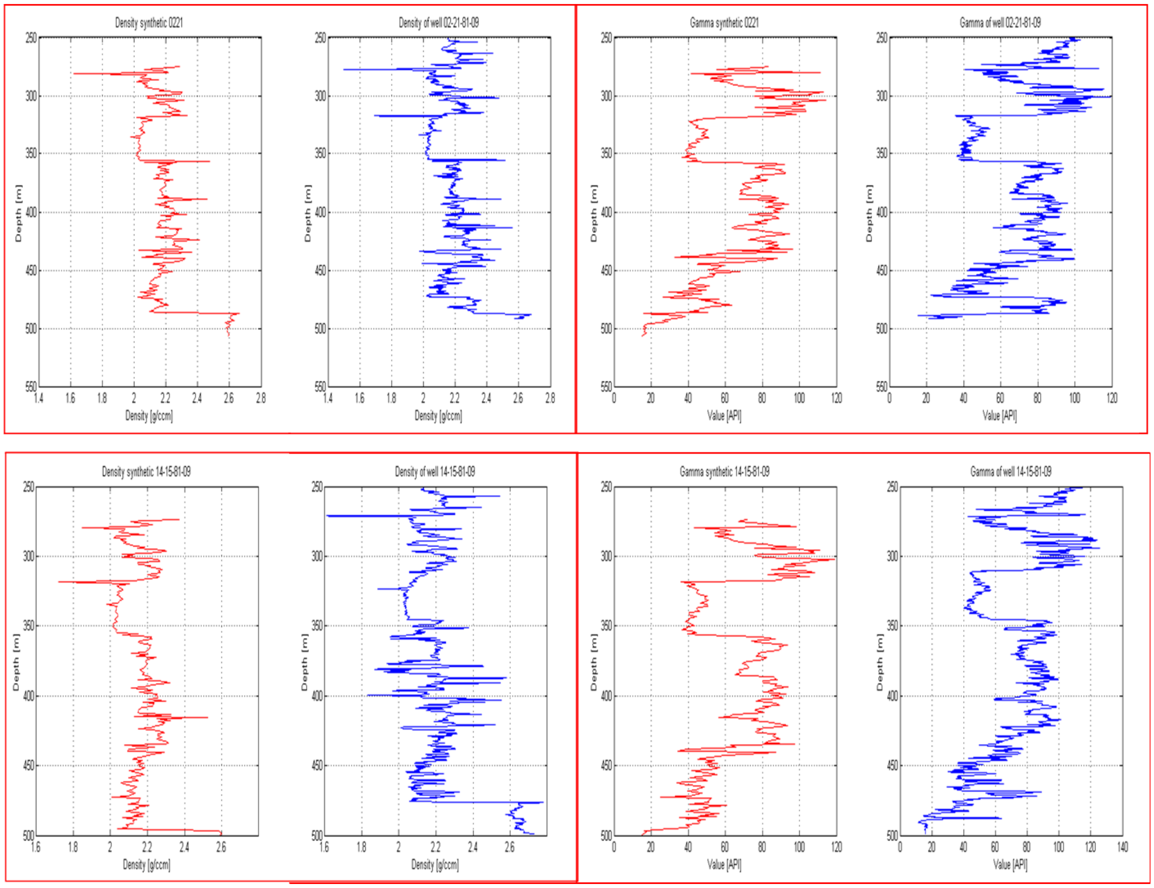

Figure 4.18: Comparison of synthetic logging data with actual data. Four sets of plots, in clockwise direction, are density of 0221, gamma of 0221, gamma of 1415, density of 1415. Red curves indicate synthetic data, while blue curves represent actual data.

Chapter 5

Zero-offset VSP processing and simulation

Vertical Seismic Profiling places receivers directly in subsurface that provides possibilities to approach or even touch subsurface targets. Besides being functioning as a tie between surface seismic and borehole log, this ‘in situ’ seismic measuring provides superiorities in presenting seismic features related with minor properties variation in the vicinity of borehole where beyond well log data can reach. 4 wells in the Corner area have VSP data, and two of them are not far from our model profile. In this chapter, these VSP data are reprocessed with a modified zero-offset processing flow with purpose to identify IHS events shown in VSP data. In order to better recognize IHS features in actual VSP data, Zero-offset VSP simulation are carried out based on finite difference modeling with acoustic wave propagation, and the synthetic data are processed in the same way as actual data.

5.1 A modified zero-offset VSP processing flow

Normally, the basic aim of zero-offset VSP processing is to extract primary compressional reflected energy (Pp[1] wave) and then tie to surface seismic data to

---

[1] The first letter denotes incident wave, while the second letter represents either reflected or transmitted wave; capital letter indicates downgoing wave, while small letter represents upgoing wave; ‘P’ indicates compressional wave, while ‘S’ indicates shear wave.

recognize primary reflected wave, since Pp energy is mostly recorded in surface seismic [Marine vertical seismic profiling, 1995]. However, the aim here is to recognize IHS features in VSP section, which may present not only in the form of Pp wave, but also in forms of Ps, PP and PS. VSP data contains many kinds of energies originated from different types of contrast in elastic parameters [Marine vertical seismic profiling, 1995], Figure 5.1 schematically presents basic wavemodes possibly observed in a VSP section. The interference of different event types may result in some energy-weak but geologically meaningful seismic responses invisible, thus wavefield separation plays an important role throughout VSP processing. There are several techniques to separate wavefield based on different velocities reflecting wave types and events. FK filter and Median filter are two basic velocity filters applied on VSP data, which are nicely explained in a principle book by Bob A. Hardage (1985).

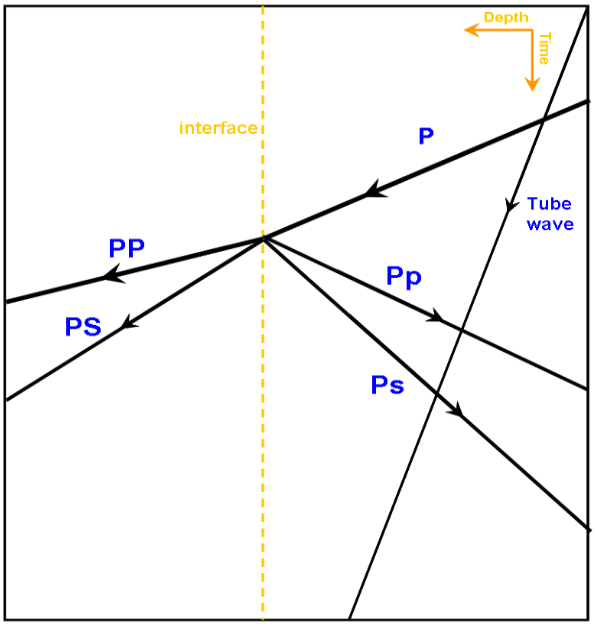

Figure 5.1: A schematic diagraph showing basic wavemodes present in a VSP section.

Based on studying [Marine vertical seismic profiling, 1995] and the VSP processing chapter in Bob A. Hardage (1985), I build a zero-offset VSP processing workflow for the purpose of investigating IHS events in zero-offset VSP section, shown in Figure 5.2. All of these processing steps are implemented with Seisspace-based ProMAX VSP. After loading stacked VSP data, traces are advanced in time by amounts of their first peak travel-times as so to align downgoing P wave. Median filter is applied on time-advanced full wavefield to extract downgoing P wave, from which deconvolution filter is designed. Then the resultant deconvolution operator is applied on the time-advanced full wavefield to remove multiples and shape wiggles. Afterwards, downgoing compressional wave is removed from deconvolved full wavefield, further separation of Ps, Pp, Ps and tube wave are done either by median filter or FK filter. Finally, separated waves are used for recognizing IHS features.

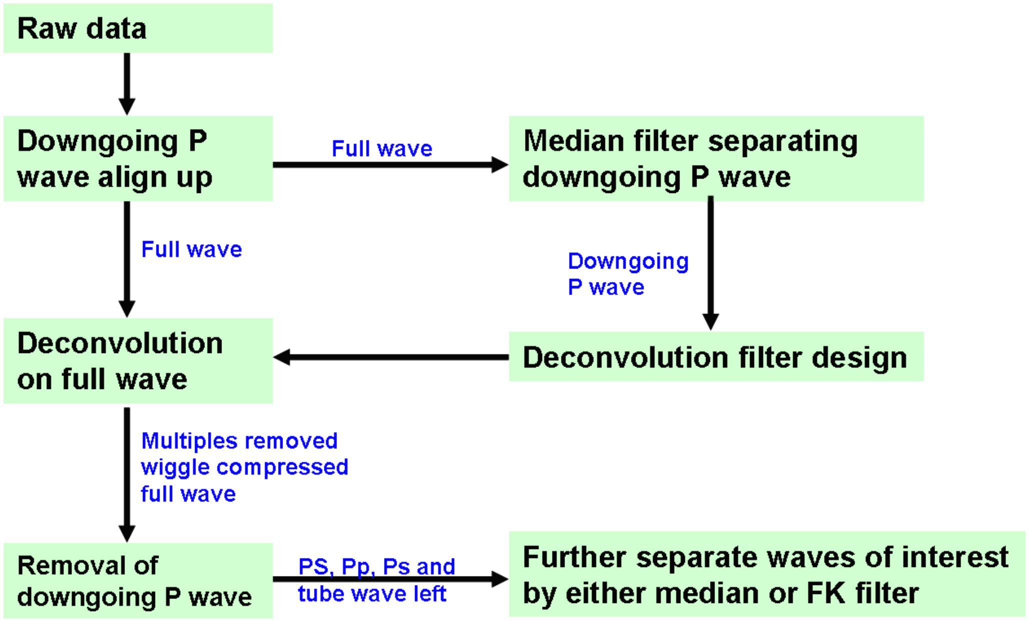

Figure 5.2: Modified kernel steps for zero-offset VSP processing with purpose to investigate VSP response of IHS

Zero-offset VSP data are available at two of wells (12-22 and 12-27) in our study area, and Figure 2.10 shows their relative positions to the selected seismic profile. Appendix figure B.8 and figure B.9 represent two cross sections along their actual and projected positions.

5.2 Interpretation of processed VSP data

Figure 5.3 shows two way travel-time sections (one with Pp aligned, the other with Pp removed) of vertical component processed zero-offset VSP of well 1222. Analyzing these two sections and comparing them with formation tops and surface seismic section (figure 4.12), several formation tops are clearly recognized. Some special features are denoted by color curves.

The green curves between Clearwater Fm Top and Wabiskaw Mbr. Top indicate converted upgoing shear wave. This is supported by: 1) they coincidence with upgoing compressional wave at recognized impedance contrast interfaces, though not all upgoing compressional wave are properly aligned; 2) they are parallel to each other and present a lower propagation velocity which is indicated by insufficient flatten with two way traveltime. These relatively pronounced converted shear wave shown in a zero-offset VSP data could imply dipping and/or scattering events present in the vicinity of borehole. And another response could also indicate dipping events near borehole is the down dipping red curve pointed at Wabiskaw Mbr. Top, which presents higher apparent velocity than compressional wave propagation due to it is over-shifted by two-way first peak travel time.

When looking at the reservoir formation (denoted by a yellow shadow), it is clear to see at least two lined up short horizons in that shadow which could indicate IHS. After Pp wave is removed, the upgoing shear wave, indicated by a green line, is present which was hidden behind Pp wave in the first section.

However, there are some events really confusing. What are those bending upwards cyan curves shown at depth of Devonian Top after Pp removed? What could the long red curve in reservoir formation represent for? Does these curves related with geological settings?

In order to better interpret processed data and relate present features to subsurface situations, we create synthetic zero-offset VSP data in our constructed model with a finite difference package developed by the CREWES, consortium for research in elastic wave exploration seismology, Calgary University.

5.3 VSP simulation and synthetic data processing

It has been explained in chapter 3, in order to obtain an accurate finite difference evaluation, some parameters need to be carefully chosen, namely finite difference evaluating time step (Δt) and space step (Δx), VSP simulating temporal sampling ($\Delta t_{sampling}$) and spatial sampling ($\Delta x_{sampling}$). By investigating the actual zero-offset VSP data, we find out the maximum temporal frequency shown in a section which has been deconvolved is 250Hz (i.e. $f_{\max} = 250Hz$). If we choose the minimum wave propagating velocity ($v_{\min}$) in subsurface as 1500m/s, according to (3-18), an appropriate finite difference space step Δx should be no longer than 1.2m (i.e. $\Delta x \le \frac{v_{\min}}{5 f_{\max}}$). And to ensure the stability of time stepping-forward method which is used here for solving wave equation, according to (3-15), finite difference time step (Δt) should be not longer than

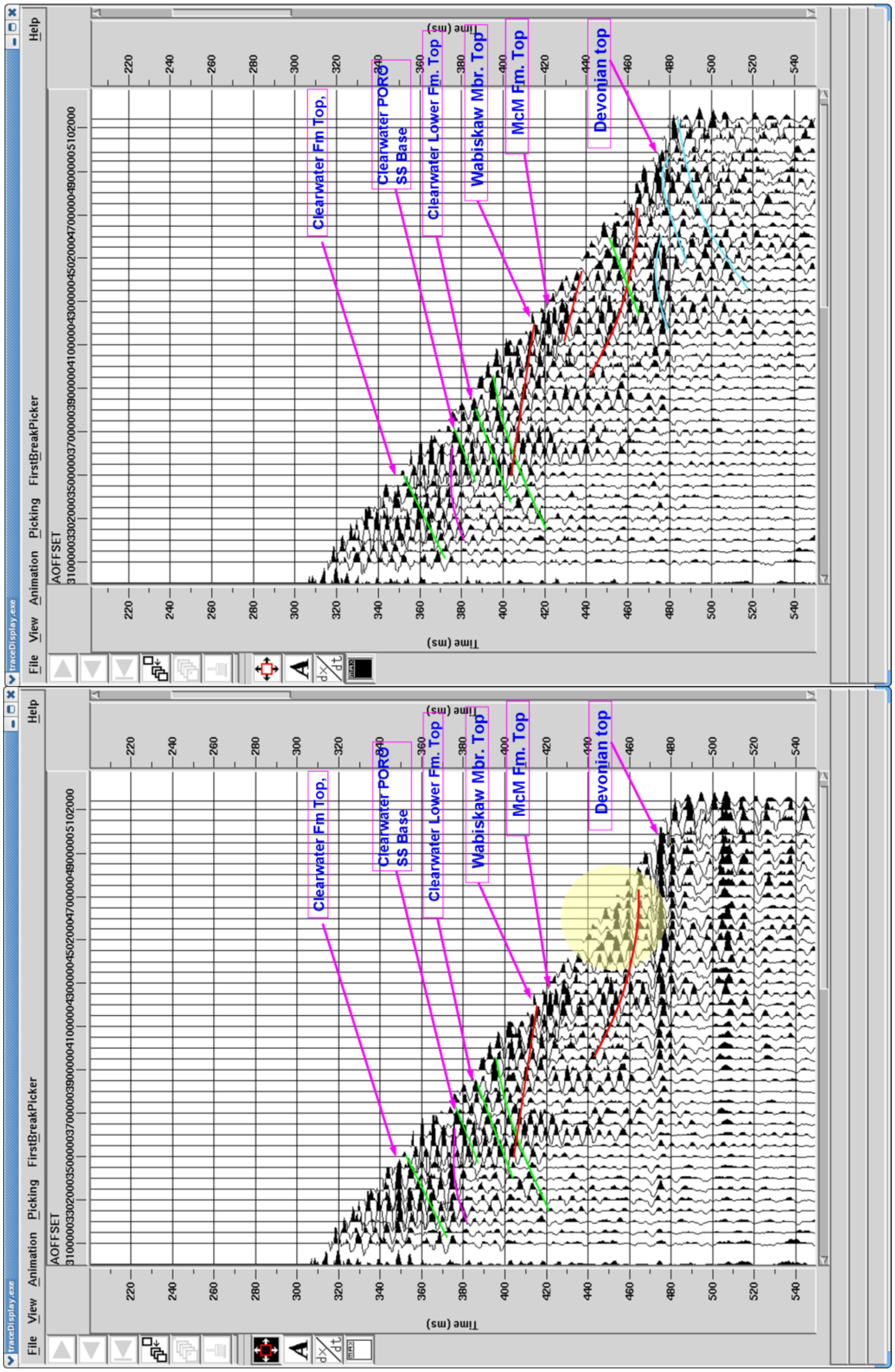

Figure 5.3: Extracted two way travel time VSP sections, the one to the left with upgoing compressional wave aligned the one to the right with upgoing compressional wave removed.

0.1ms, given the maximum propagating velocity ($v_{\max}$) equals to 3600m/s. Then considering Nyquist theorem to avoid aliasing both in time domain and space domain, the temporal and spatial sampling should satisfy:

$$\Delta t_{sampling} \leq \frac{1}{2f_{\max}} = 0.002s \ , \ \Delta x_{sampling} \leq \frac{v_{\min}}{2f_{\max}} = 4m$$

where the $\Delta x_{sampling}$ corresponds to geophone spacing, and $\Delta t_{sampling}$ corresponds to recording time samples. For our simulation, we choose: Δx =1m, Δt =0.1ms, $\Delta x_{sampling}$=2m, $\Delta t_{sampling}$=0.001s

It is also allowed to define finite difference evaluating boundary either as absorbing or non-absorbing, we choose three sides to be absorbing and the top boundary not be, which enable source to be put on the surface. In addition, for higher accuracy reason, we choose 9 points Laplacian operator approximation. A filter or wavelet can also be defined either with zero phase or minimum phase. Since outputs of the simulation include seismogram and impulse signature, which is seismic response of an impulse source, it is always possible to calculate seismogram afterwards by convolving the impulse signature with a desirable filter/wavelet.

Simulation are carried out at projected position of 1222 and that of 1227, hereafter a bandpass filter [3 8 200 250] is used to convolve with corresponding impulse signatures to obtain seismogram. After this, synthetic VSP data are processed in the same way as actual data. The comparison between synthetic processed data with actual processed data is proceeded.

5.4 Comparison of processed actual data and synthetic data

Figure 5.6 is processed two-way travel time sections of synthetic data at projected position of well 1222, compared with Figure 5.3, the synthetic section is pretty clean, only those aligned upgoing Pp wave indicating some main formation tops are present, converted waves and waves related with dipping or scattering condition in vicinity to borehole are all invisible. Since the finite difference simulation applied here is based on acoustic model dealing with acoustic wave equation, no elastic parameter is involved thus converted wave can not be generated. By looking at Appendix figure B.8, vicinal conditions around real position are more complicated that projected position, which could result in some scattering events in actual data. And also observed from the velocity model (Figure 5.4), reservoir around projected 1222 has very weak velocity contrast that leads to few events. Though the vicinal conditions of well 1227 is more comparable to its projected position than the case of 1222, the acoustic model based finite difference simulation and also weak velocity contrast within reservoir result in few events except several aligned upgoing compressional wave reflected from formation tops.

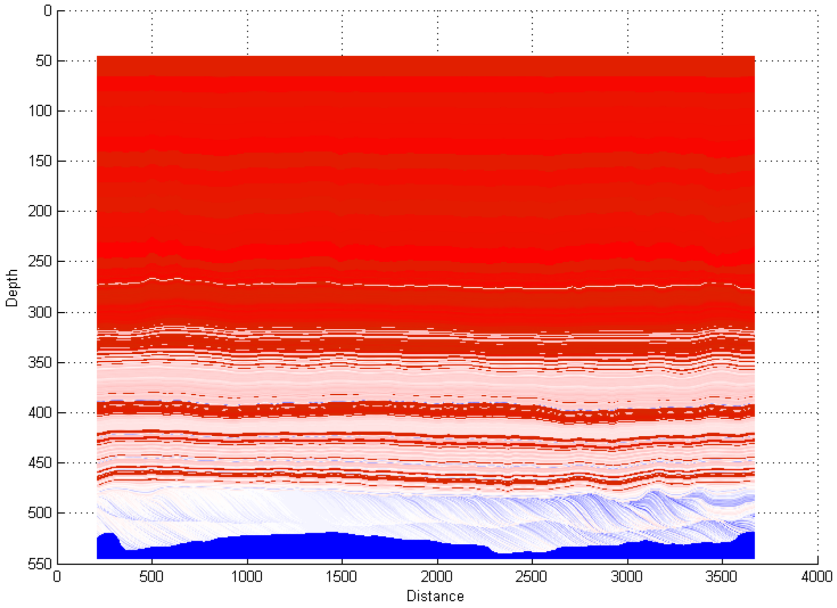

Figure 5.4: Velocity model section

Since both positions of projected wells correspond to area in the reservoir with weak velocity contrast that leads to small reflectivity. In order to investigate whether features of IHS can be reflected in acoustic model based zero-offset VSP simulation, we place a reference vertical well at a position where it goes through the reservoir formation with relative high velocity contrast. The processed synthetic section is shown to the right side of Figure 5.6, while the left one is based on the same model except replacing velocity field in point bar deposits by a constant velocity. Comparing responses from reservoirs with different velocity fields, IHS leads to VSP responses slightly different from those based on constant velocity field, but it is difficult to give direct correspondences based on the current situation.

Although IHS features in actual data are not apparently shown in synthetic data, those pronounced aligned compressional wave are consistent with features presented in actual data related with subsurface structures, which justify the validity of the constructed model once more. Based on logging data, density is a better lithology indicator and density contrast is more significant than velocity contrast, so an elastic model based finite difference will be more valuable for simulating zero-offset VSP data to investigate IHS responses, whose results will reflect more events like amplitude variation, converted wave etc.

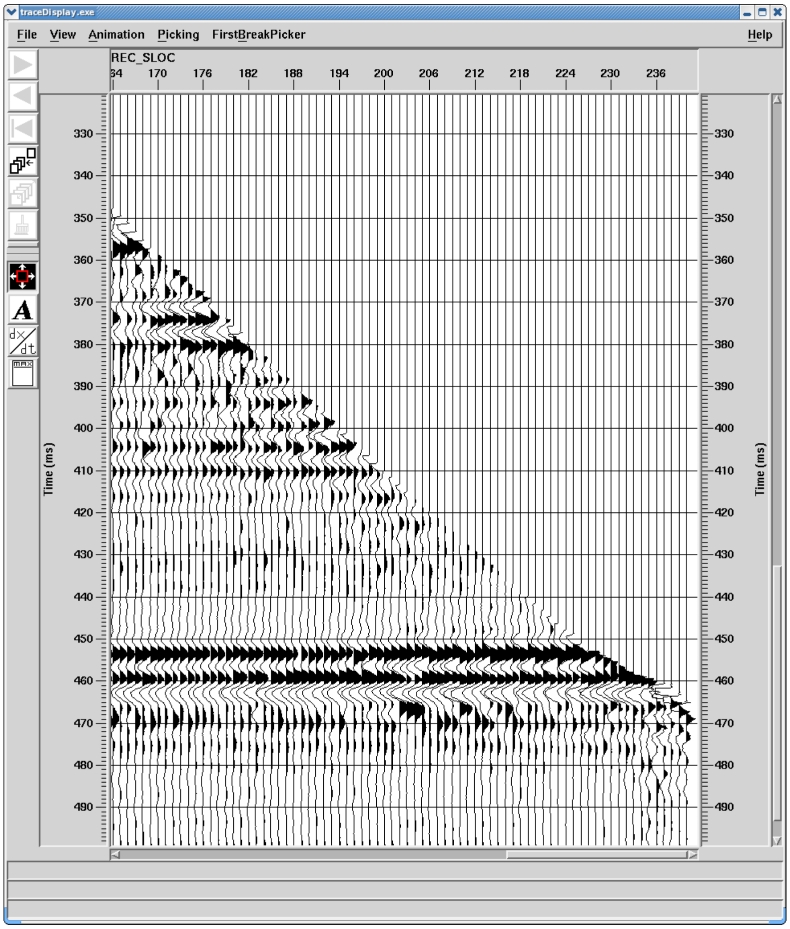

Figure 5.5: Extracted two way travel time section of synthetic data at projected position of well 1222.

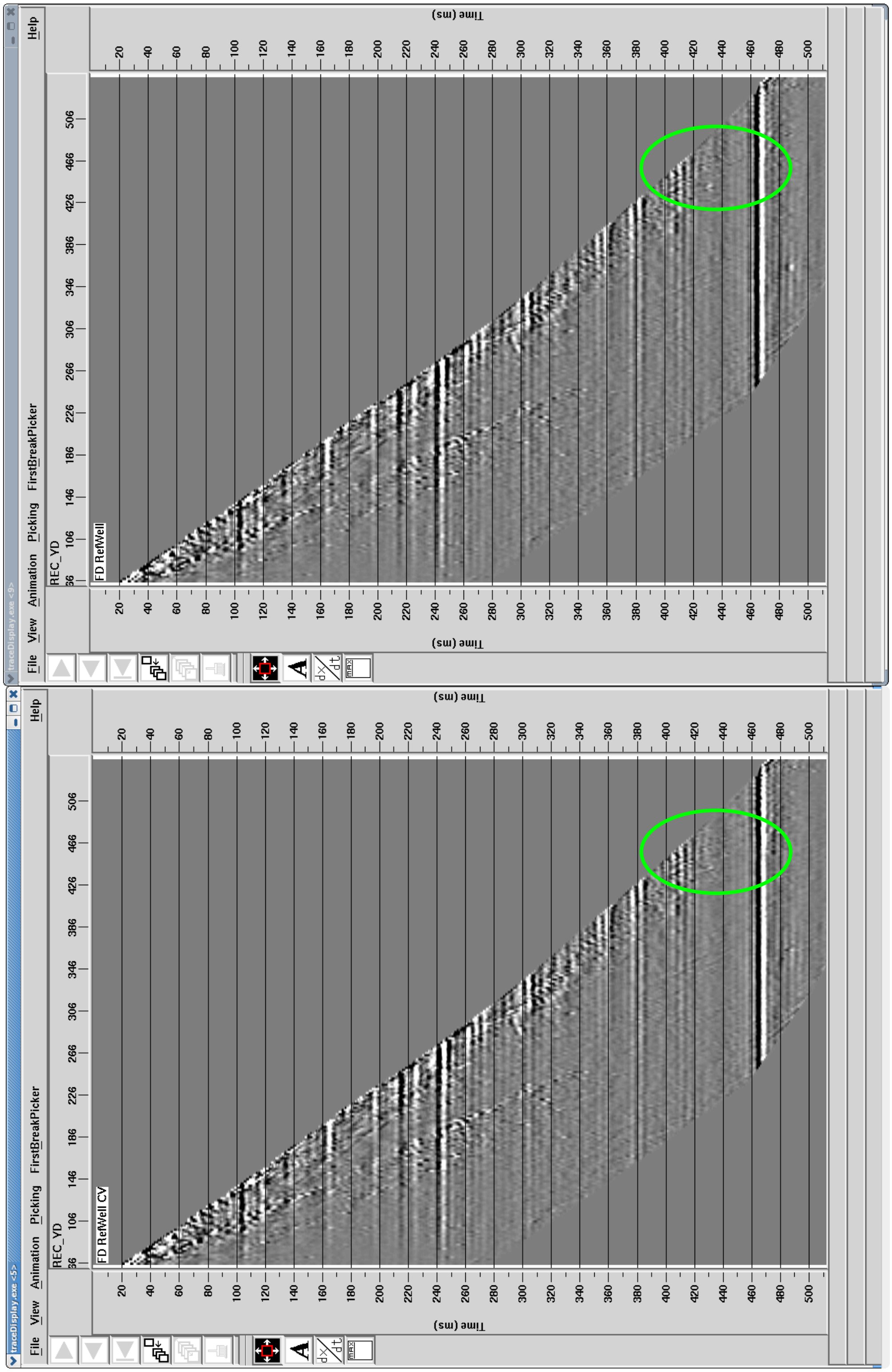

Figure 5.6: Processing results of zero-offset simulated VSP at reference well. The one to the left is based on a modified model with replacing velocities in point bar deposit by a constant, while the one to the right is based the true constructed model.

Chapter 6

VSP simulation with receivers laterally distributed

In chapter 5, we simulate zero-offset evaluations at three positions in the constructed model with intention to relate IHS settings with desired VSP responses. But due to limitation of zero-offset VSP deployment and only velocity contrast involved in wave propagation evaluation, it is difficult to draw clear relation between reservoir heterogeneities and synthetic VSP responses. While in this chapter, we simulate different scenarios of VSP deployments by locating receivers in horizontal wells at different levels, proceeding by comparing their travel-time curves we try to deduce a relation between heterogeneities and these travel time variations. Simulations in this chapter can be put in two categories, one is point source offset VSP, i.e., appoint a point source near surface and situate receivers in reservoir laterally; the other is plane wave source VSP simulation, i.e., assuming plane wave can be generated from surface and receivers located laterally in reservoir.

Parameters of finite difference evaluation are kept the same as those used for zero-offset simulation in last chapter, i.e., Δx =1m, Δt =0.1ms, $\Delta x_{sampling}$=2m, $\Delta t_{sampling}$=0.001s. In order to locate source on surface, we choose three sides of evaluating boundaries to be absorbing and the top boundary not be; for higher accuracy, we are using 9 points Laplacian operator approximation.

6.1 Point source & receivers laterally distributed VSP

We draw two curves H1 and H2[1] with horizontal parts at depth of 505m and 496 respectively in the model (Figure 6.1) to **indicate a pair of SAGD wells drilled in the reservoir.** Though the length of SAGD well-pair is around 1000m, this does not limit us to extend our visual wells cross the whole area of interest. Two rig sources are located at projected positions of well 1222 and 1227 ,and for the same concern as in zero-offset VSP simulation, another rig source is situated at reference well which passes through reservoir with higher velocity contrast. Receivers are located along H1 and H2 with interval of 2m. A simulating result is shown in Figure 6.2. Reflections are dominated by strong refraction energies. It is difficult to recognize some features related with IHS patterns in all three cases. In addition, since wave velocity are much higher in Devonian top, around 4500m/s, than in reservoir, about 2800m/s, according to Snell rule, the critical angle is: $\sin^{-1}\frac{2800}{4500}=38.5^{o}$. Thus the image extent is highly limited, e.g., Devonian top at depth around 500m in measuring depth, the maximum extent that reflections can reach is: $500m\times tg38.5^{o}\approx 400m$.

6.2 Plane wave source & receivers laterally distributed VSP

6.2.1 Plane wave

Plane wave is a theoretical wave whose wavefront are infinite parallel planes normal to the velocity vector. In the constructed 2D model, plane wave source is implemented as a set of horizontal aligned point sources shot simultaneously.

Figure 6.3 schematically demonstrates how plane wave contribute to a travel-time recorded by single receiver (R in this case). The orange dash hyperbola is a purely imaginary common receiver (R in this case) gathering given sources are shot consecutively. The final travel time recorded by receiver R essentially is a lateral stack of the orange dash hyperbola (common receiver gathering), and only the stationary part (schematically marked by green shadow) mainly contribute to the final first arrival. Thus, the first arrival travel-time picked at receiver R is not exactly equal to the one way vertical incidence travel time from A to R, but a smeared travel time within a small

---

[1] Though H1 and H2 represent a pair of SAGD wells, in rest of the context, H1 and H2 only indicate horizontal part of the well, excluding vertical and deviating part.

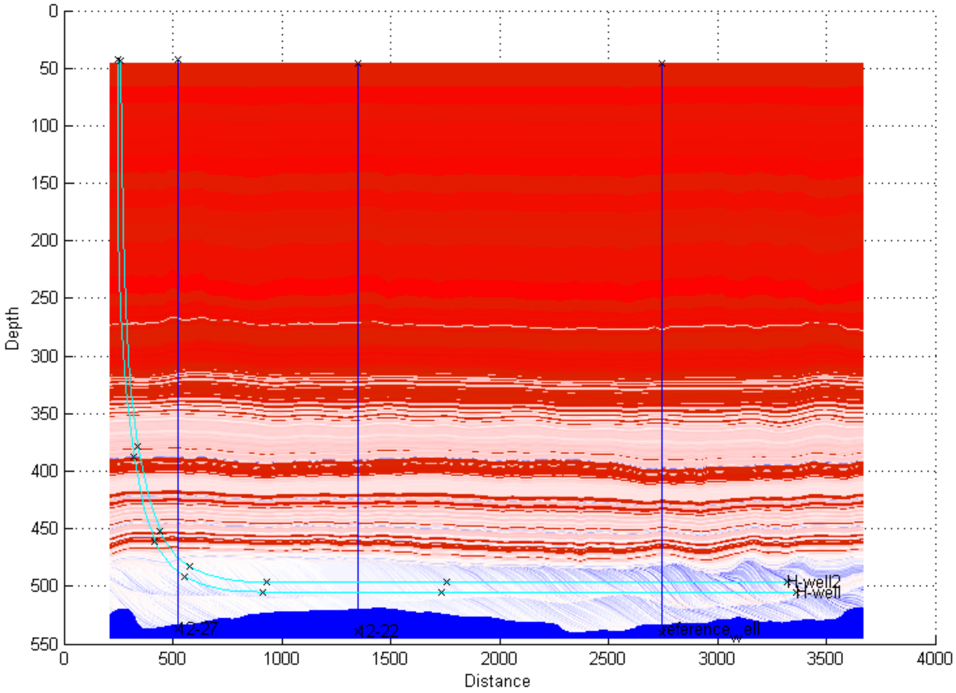

Figure 6.1: Velocity model with indication of horizontal wells and point sources

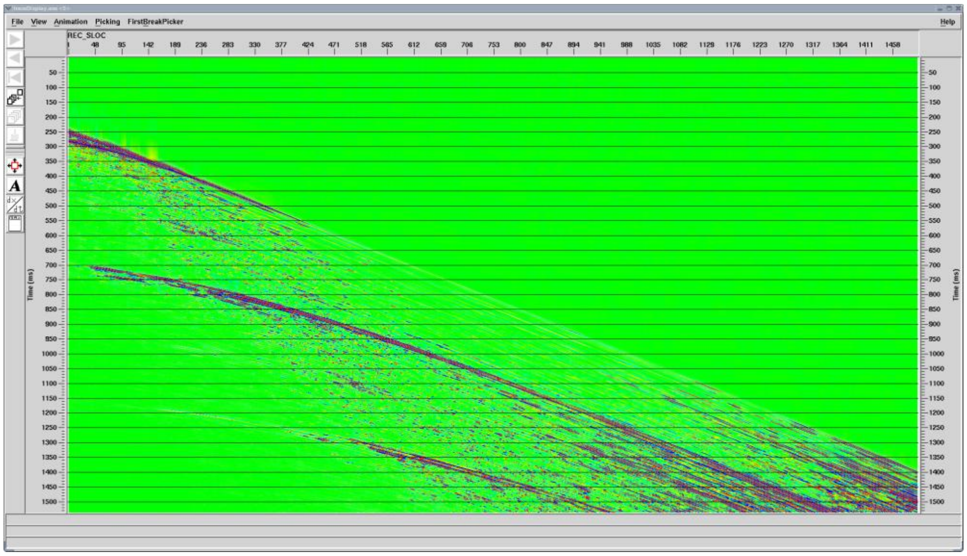

Figure 6.2: Results of point source at well head of H1 with receivers laterally distributed VSP

region. The size of the region relies on the extent of stationary part, out of which travel time will not contribute to the smeared travel time as being largely out of phase with the vertical incidence travel time. In this simplified diagraph, only shots A, B and C contribute to the first arrival travel-time recorded at receiver R, even though all shots are shooting. This enables us to investigate first arrival travel-time of all receivers at one time by shooting all sources simultaneously rather than simulating vertical incidence at each source point. Though the vertical incidence simulation is more precise, it will take too much computing time. One should be aware that simulating with plane wave source requires relative flat overburden above receivers, and also a recorded first arrival travel-time at one receiver is smeared with other travel time if their stationary parts partially overlapped.

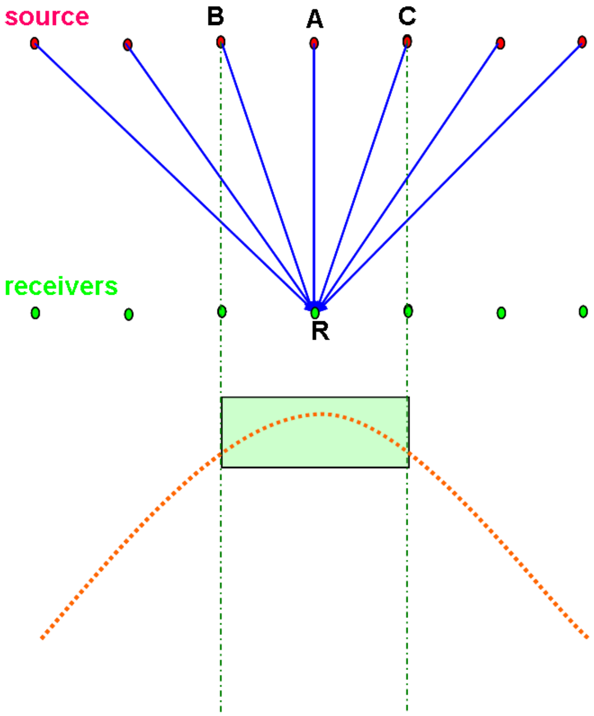

Figure 6.3: A schematic diagraph illustrates relationship between plane wave and the first arrival travel-time recorded by a single receiver.

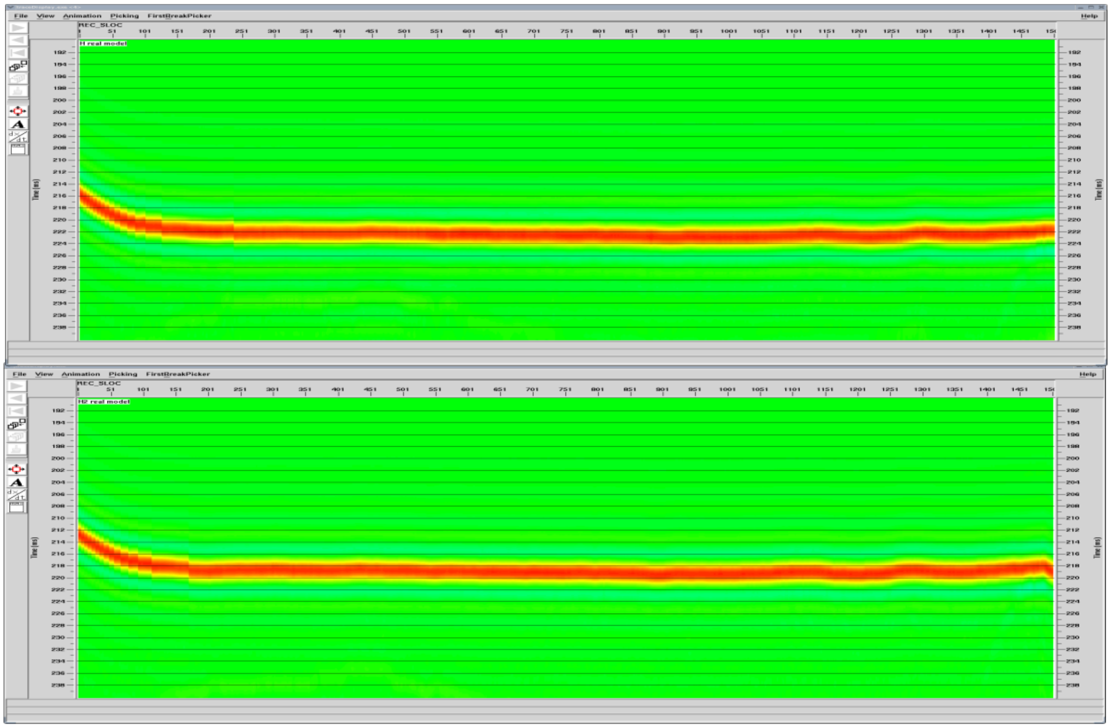

Figure 6.4: Synthetic VSP data with plane wave source and receives laterally distributed, H1 is on top, H2 is at bottom.

6.2.2 Simulation based on original model

In our simulations, line source is defined across the section with source interval of 2m, and receivers are located along H1 and H2 with interval of 2m. Synthetic results of H1 and H2 are shown in figure 6.4.

Considering the plane wave source and laterally distributed receivers, if no heterogeneities presents in these two levels, the recorded first arrival travel-time of each vertical incidence should be the same given the same offset, which would result in a straight time variations line. While if heterogeneities exist, e.g. interbedded mudstone and sandstone, the heterogeneous property distribution will lead to different ray paths between shots and receivers, hence different travel time shown by travel-time variation curve. Therefore, analyzing behaviors shown on the travel-time variation curve can help to investigate and characterize heterogeneities.

Curve 1 and curve 2 shown in Figure 6.5 present variation of first arrival travel-time along H1 and H2 respectively. Observing these two curves, it can be noticed that: variation of first arrival travel-time along a horizontal well can be decomposed to a general trend change, which reflects background property changes above, e.g. overburden layers, and oscillations (higher order amplitude variations) which imply specific property variations near the well, e.g. point bar deposits in the reservoir. By comparing curves of first arrival travel-time located at different depth, it is possible to exclude affects stem from common background property changes, and enables us to relate travel-time variations with local properties only. Curve 3 in figure 6.5 presents variation of travel-time difference between H1 and H2, which potentially indicates heterogeneities in between. Curve 4 is accumulative slowness between H1 and H2 which implies travel time of vertical incidence from H2 to H1, each value is calculated by multiplying grid step with vertical accumulation of slowness. It directly denotes lateral distribution of velocity. Consistence between the shape of curve 3 and curve 4 confirm that the variation

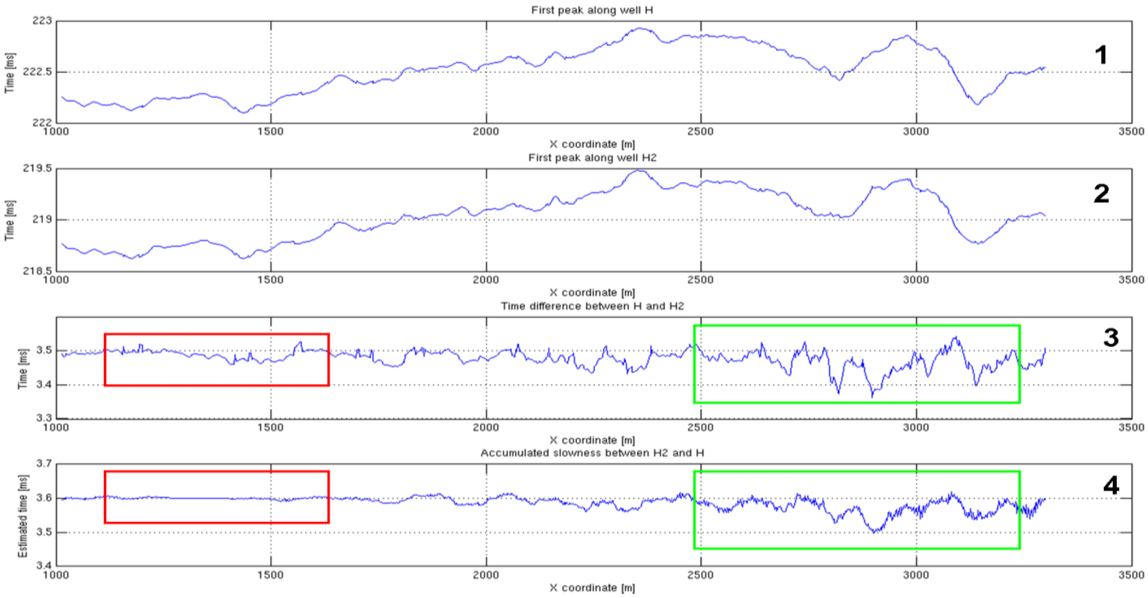

Figure 6.5: Comparison of first arrival time at H1 and H2. The first curve represents first arrival time along H1, the second curve indicates first arrival time along H2, the third curve is travel-time differences between H1 and H2, last curve is lateral variation of accumulative slowness between H1 and H2, which im**plies theoretical travel time** differences between H1 and H2 given vertical ray path. Travel time evaluations are based on original model.

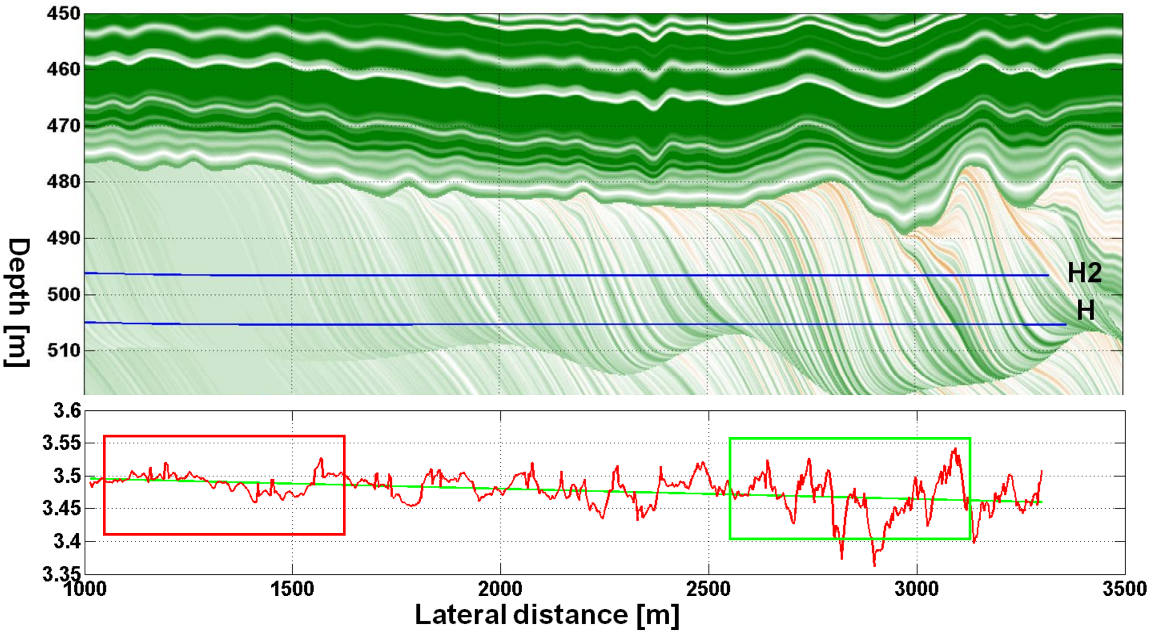

Figure 6.6: Comparison of travel-time difference and velocity distribution between H1 and H2

along curve 3 are mainly due to heterogeneities between H2 and H1 rather than topography of top McMurray or overburden layers, and further support the validity of using travel time difference to investigate velocity distribution.

Since distance between H1 and H2 is constant, the large value of travel-time difference indicates lower average velocity in between, while small travel-time difference implies higher average velocity in between. In the reservoir model, clay and muddy deposit owns higher velocity than sandy deposit does, therefore high amplitude on curve 3 indicates higher proportion of sand, while low amplitudes indicate higher proportion of clay. These correspondences are also reflected in the Figure 6.6.

Besides amplitude correlation, the frequency of oscillations shown on the travel-time difference curve closely relate with occurrences of inclined units in the space between H1 and H2. Places in reservoir model with weak velocity contrast (marked by a red box) correspond to segments of variation curve where oscillations are few and small; while places with high velocity contrast (marked by a green box) relate with segments of significant oscillations.

In addition, the size of a single envelope (*e*) on curve 3 possibly indicates the lateral extent (*l*) of an inclined unit. And as the distance (*d*) between H1 and H2 is known, the dipping angle (α) of the inclined unit could be approximated by: $\arctan\frac{d}{l}$, given the inclined unit reaches both H1 and H2. Alternatively, if the dipping angle (α) is known by other means (e.g. well logging), we are able to predict the connectivity between H1 and H2 by comparing d with $l \cdot \tan\alpha$, which could be valuable information for the SAGD.

It is worthwhile to mention that the accuracy of seismic acquisition can reach is 0.01ms[1]. Valuable amplitudes of vacillations shown along curve 3 which potentially correspond to IHS patterns are in the order of 0.05ms, therefore these meaningful responses can be distinguished from noise.

6.2.3 A trial to smooth the curve of first arrival travel-time

It is observable that there are several sharp jumps on the variation curve of travel-time difference, and we can also see several uncontinuous points on curves of first arrival travel-time, Figure 6.7 Although these points have little influence on the conclusion we have already obtained, we try to remove them with intention to better correlate with IHS patterns by fining model grid, from $1m \times 1m$ to $0.25m \times 0.25m$, and reducing receiver step, from *2m* to *1m*. Re-calculated curves are shown in Figure 6.8, from which we can see refining grid and spatial sampling does not improve continuity of the first arrival travel-time curve, those jumps are still there even without any change. Therefore, those jumps might be due to finite difference method or the picking algorithm itself which is beyond the scope of this thesis. Alternatively, this confirms the grid and spatial sampling we used before are correct and sufficient enough.

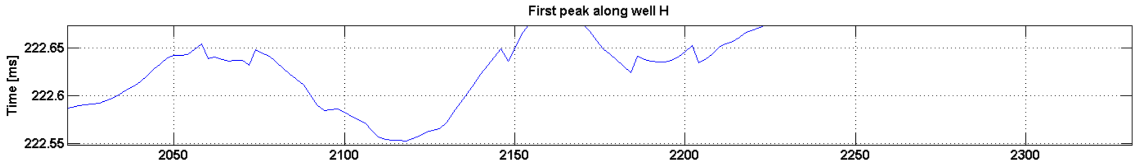

Figure 6.7: A zoomed in segment of the first arrival travel-time variation curve. Several uncontinuous points are observable.

---

[1] This value is mentioned in: Technical requirement for GOC monitoring in horizontal wells by direct-arrival travel-time inversion, Rigmor M. Elde, Einar Maland, Steen A. Petersen, 1992, SPE Evaluation.

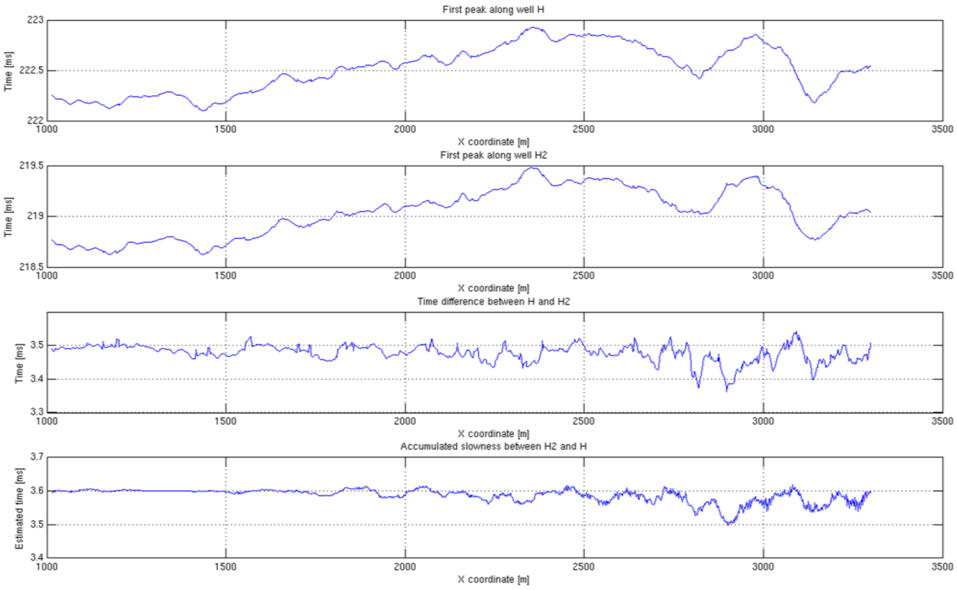

Figure 6.8: Comparison of first arrival time at H1 and H2, with model grid $0.25m \times 0.25m$, receiver step of 1m.

6.3 Conclusion and comment

Based on acoustic finite difference modeling, comparing travel-time difference between two horizontal wells provides a potential method to investigate heterogeneities of point bar deposits. Frequency of oscillations shown on a curve of travel-time difference represents occurrences of IHS; given the dip of an inclined unit, local connectivity can be predicted by the width of a oscillation. These could provide valuable information for SAGD production.

Considering impedance contrast within McMurray is dominated by density, if an elastic finite difference modeling is available, results of simulation will be more fruitful. For plane source VSP simulation, besides travel-time analysis, we will be able to investigate amplitudes variation, which could reflect more information about the medium. And for point source zero-offset and non-zero-offset VSP, there will be more events shown by wave conversion in synthetic data, providing more possibilities to relate VSP responses with IHS patterns. In addition amplitudes analysis would also be helpful to identify IHS patterns from VSP responses.

Chapter 7

Conclusions and recommendations

The aim of this thesis is to investigate correspondences between VSP events and IHS features in point bar deposits. Before the simulation based investigation proceed, a near-to-realistic model need to be built. Therefore, both conclusions and recommendations are divided into two parts.

Conclusions for IHS oriented point bar model building: we are able to construct IHS oriented point bar deposits from borehole data. By decomposing logging data into BPF and BVF and examining geometrical relationship between inclined units and borehole, IPF and IVF can be derived from BPF and BVF. IPF represents influence of gravity on point bar deposition, while IVF indicates how current affects point bar deposition. Combing IVF, IPF and sigmoid shape of inclined units, a local realistic point bar deposits can be created. The local point bar deposit is then extended to a global point bar deposits by constructing a global IVF which preserves characteristics of IVF. The validity of the constructed model is evaluated by comparing synthetic surface seismic and synthetic logging data with actual data. They both present high consistence with features reflected in actual data.

Recommendations for model building: in order to make the model even more precise, depositional processes based numerical simulation will be required, and it should be implemented in 3D.

Conclusions for simulation part: our aim of relating VSP responses with IHS features is fulfilled by comparing variation of travel-time difference with velocity model, given plane source wave and laterally distributed receivers. It turns out that the oscillating frequency shown on the curve of travel-time difference indicates occurrences of IHS, and a single oscillation width could imply lateral extent of an IHS. Given the thickness and dipping angle of inclined units, it is possible to predict connectivity between two levels (tow horizontal wells).

Recommendations for simulation part: according to logging data, density is a better lithology indicator than velocity, thus impedance contrast is more determined by density contrast. If elastic modeling is available, heterogeneities characterization by acoustic travel-time can be improved/ enhanced by analyzing amplitudes variation and wave conversion that would contribute to more precise identification and characterization.

References

Aki K., and P. G. Richards, 2002, Quantitative seismology: University Science books.

Derald G. Smith, 1988, Tidal bundles and mud couples in the McMurray formation, northeastern Alberta, Canada: Bulletin of Canadian Petroleum Geology, vol. 36, No. 2, P. 216-219.

Derald G. Smith, Stephen M. Hubbard, Dale A. Leckie and Milovan Fustic, 2009, Counter point bar deposits: lithofacies and reservoir significance in the meandering modern Peach River and ancient McMurray Formation, Alberta, Canada: Sedimentology, 56, 1655-1669.

Gary F. Margrave, 2003, Numerical Methods of Exploration Seismology with algorithm in Matlab, The University of Calgary, Chapter 3: Wave propagation.

Gary, Greig T., Hoehn, M., Jordan, O., Brekke, H., 2011, Master DG2 Geosciences documentation (Statoil internal document);

Gerrit Toxopeus, 2006, Simulating migrated and inverted seismic data for enhanced reservoir characterization, PhD. Dissertation, Delft University of Technology.

Gerrit Toxopeus, Jan Thorebecke, Kees Wappenaar, Steen Petersen, Evert Slob, Jacob Fokkema, 2008, Simulating migrated and inverted seismic data by filtering a geological model: Geophysics, 73, P. T1-T10

Kelly K. R., Ward R. W., Treitel Sven, and Alford R. M., 1976, Synthetic seismograms: a finite-difference approach: Geophysics, vol. 41, P. 2-27.

Leismer Demonstration Project SAGD Summery & Overview, Statoil Canada Limited;

Lines L. R., Slawinski R., and Bording R. P., 1999, A recipe for stability of finite-difference wave-equation computations: Geophysics, 64, 967-969.

Mitchell A. R., and Griffiths D. F., 1980, The Finite Difference Method in Partial Differential Equations: John Wiley and Sons.

Richard G. Thomas, Derald G. Smith, James M. Wood, John Visser, E. Anne Calverley-range and Emily H. Koster, 1987, Inclined Heterolithic stratification – terminology, description, interpretation and significance: Sedimentary Geology, 53, 123-179.

Steen A. Petersen, 1999, Compound modeling – a geological approach to the construction of shared earth models: EAGE 61st conference & exhibition, Session 5-12.

Steen A. Petersen, 2004, Optimization strategy for shared earth modeling: EAGE 66th conference & exhibition, Session P257.

Steen A. Petersen, 2006, Natural perturbations of shared earth models: EAGE 68th conference & exhibition, Session E029.

Steen A. Petersen, Ø. Hjelle and S. Lund Jensen, 2007, Earth modeling using distance-fields derived by fast marching: EAGE 69th conference & exhibition, Session D024.

Sheriff R. E., 2001, Encyclopedic dictionary of applied geophysics: SEG.

Appendix A

Another way to construct local point bar deposits

It is mentioned in the 4.2.1.2, given a linear BPF, the sigmoid shape of inclined units (Figure 4.8) results in the deviation between 'recorded' log (shown as solid squeezed sigmoid curve to right side of figure, log is supposed to be equal to BPF) and BPF (black dash straight line cross with log), in order to reduce this deviation, some adjustment can be made either on BPF or BVF. Adjustment on BVF has been deeply discussed in 4.2.1.2, in this appendix some comments will be made for the other method.

Actually, instead of saying adjusting BPF, it is more precise to state modifying IPF. Since BPF is derived from logging data directly by linear curve fitting, it should not be changed. Observing the diagram to the right side of Figure 4.8, it can be noticed that modification on BVF talked in previous section is shifting points on this solid squeezed sigmoid curve either down or up along vertical direction to approach the black dash line. Therefore, it is natural to expect that shifting those points laterally could also be a way to reduce deviations between the dash line and the sigmoid curve. In fact, shifting points vertically implies modifying sample steps between points, while moving points laterally denotes modifying property values and keeping their steps. This value-modified and step-kept method also leads to modify 'property density' (property variation per unit arc-length) so that compensate the influence of sigmoid curve on 'property density'. To be specific, due to the shape of sigmoid curve, ‘property density’ is forced to increase at distant parts while decrease in the central part; a desirable effect is to compensate this distant-increase-central-decrease variation of property function. In order to achieve such an effect, the IPF has to be a curve that its first derivative times derivative of sigmoid curve equals to the slope of the blue dash line. This method is applicable in this simple case in which BVF equals to zero, i.e., IPF does not shift along the blue dash line (precisely speaking, IPF should shift along the sigmoid curve rather than the straight line, but sigmoid curve is approximated to a straight line if its dip is small), IPF is only needed to modify once. When it comes to IHS structures’ construction, IPF has to be adjusted after every shift indicated by IVF which would result in highly computational cost.

Appendix B

Cross sections along well positions and projected positions

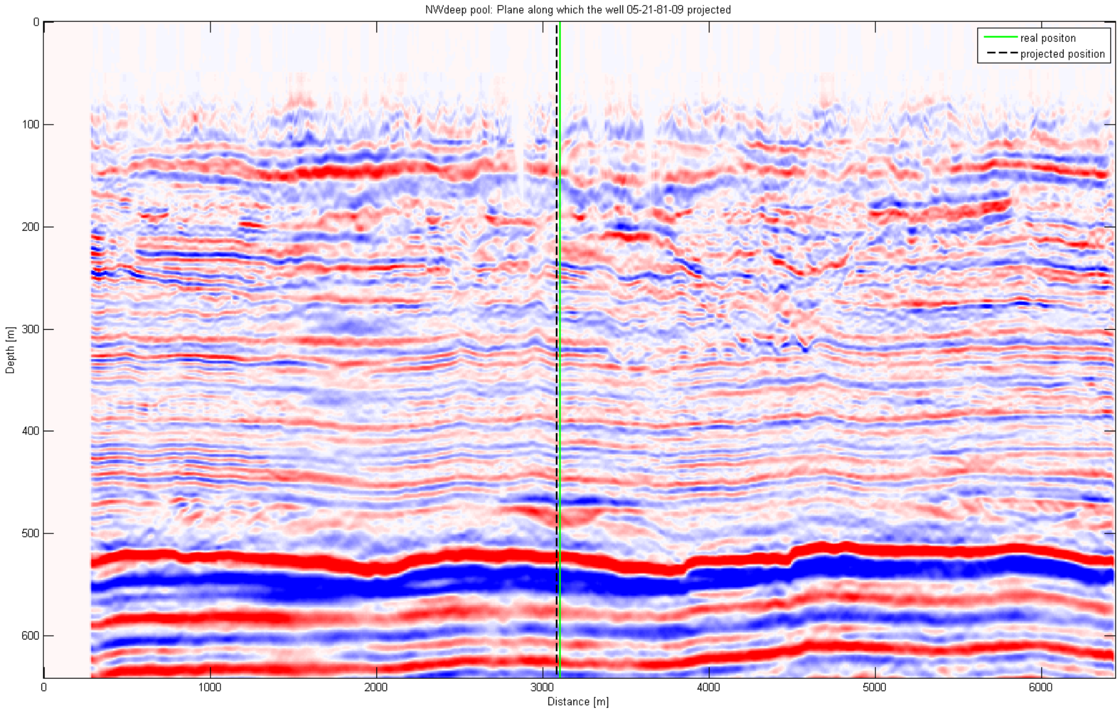

Figure B.1: Cross section along well 0521 and its projected position.

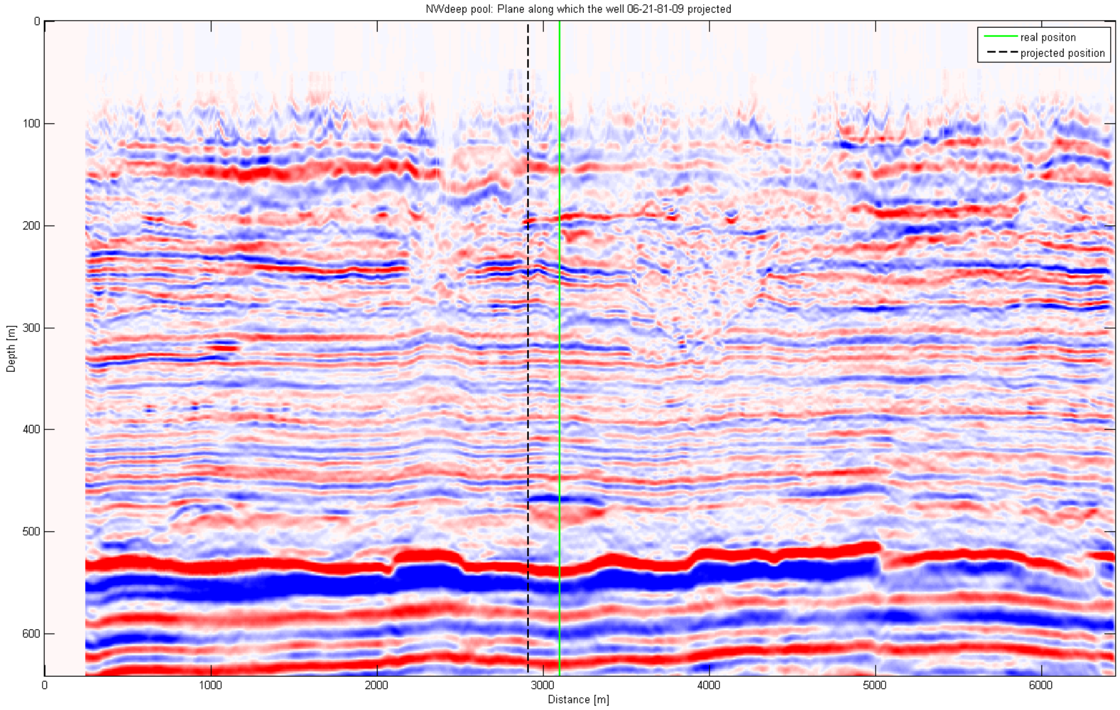

Figure B.2: Cross section along well 0521 and its projected position.

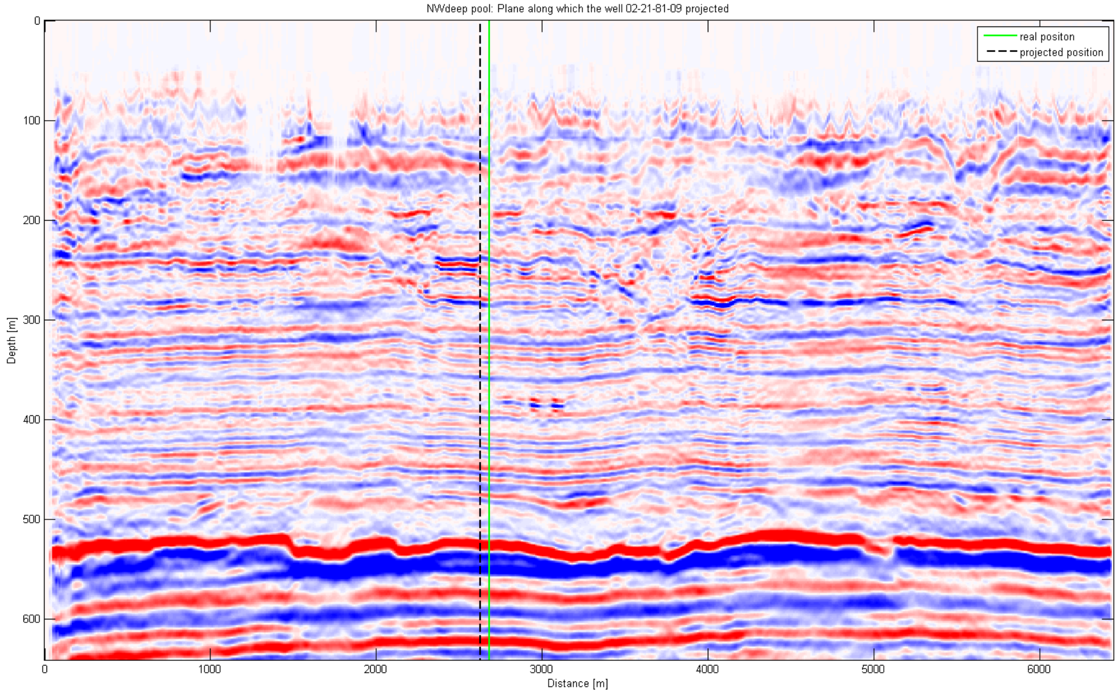

Figure B.3: Cross section along well 0221 and its projected position.

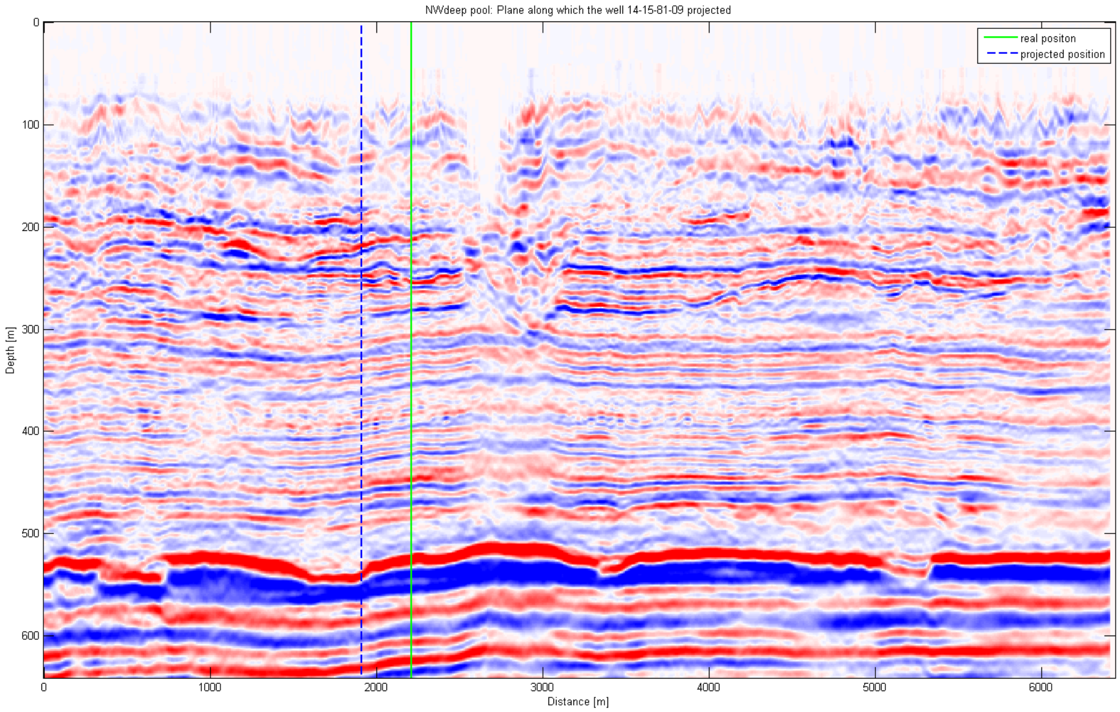

Figure B.4: Cross section along well 1415 and its projected position.

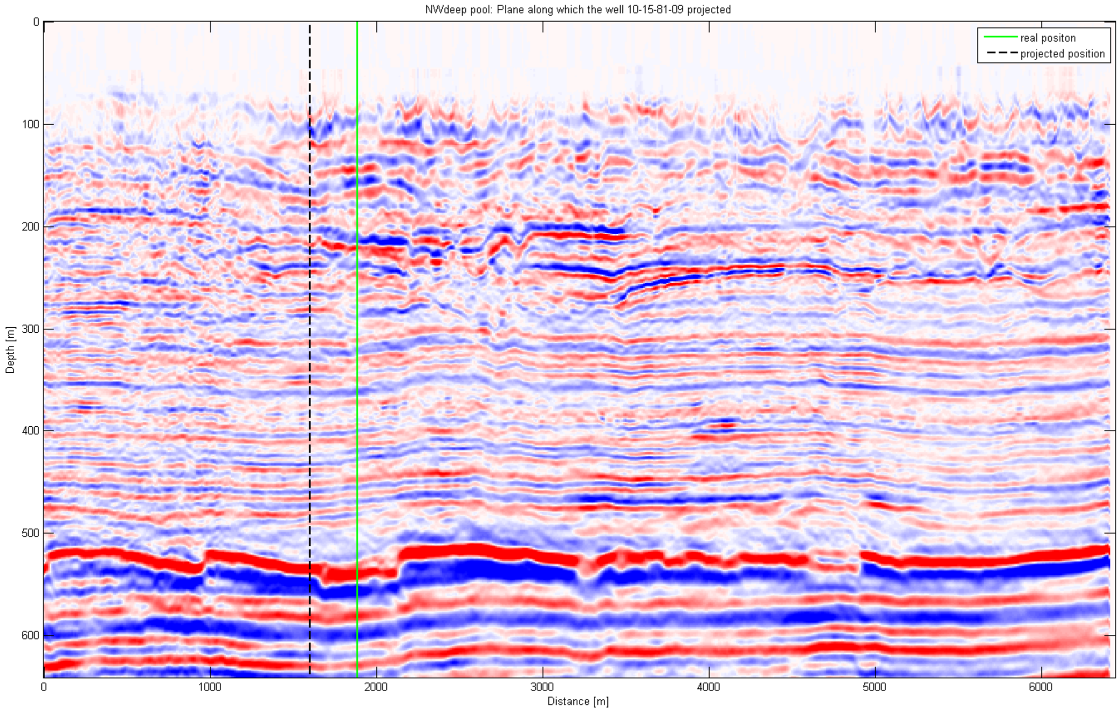

Figure B.5: Cross section along well 1015 and its projected position.

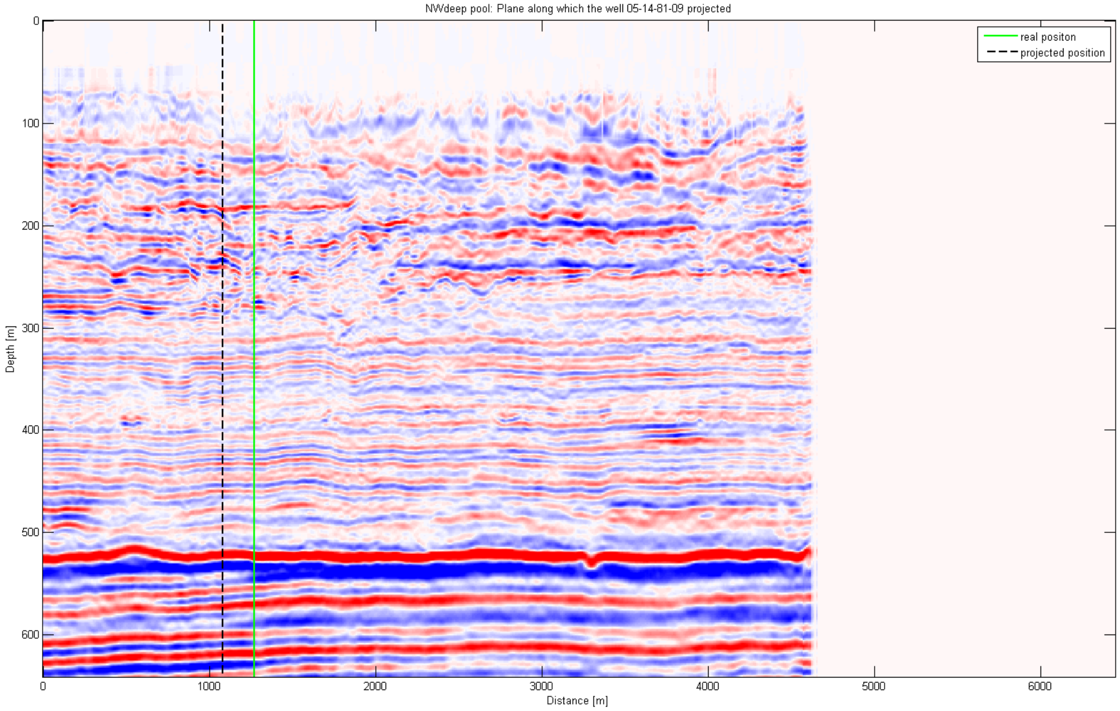

Figure B.6: Cross section along well 0514 and its projected position.

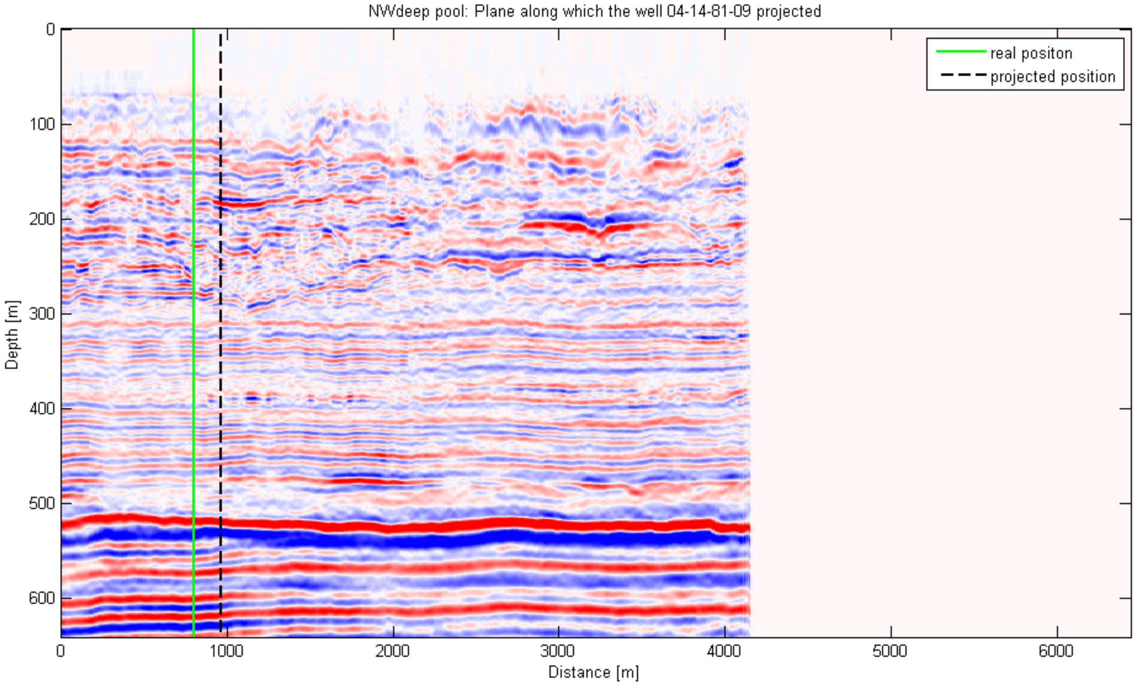

Figure B.7: Cross section along well 0414 and its projected position.

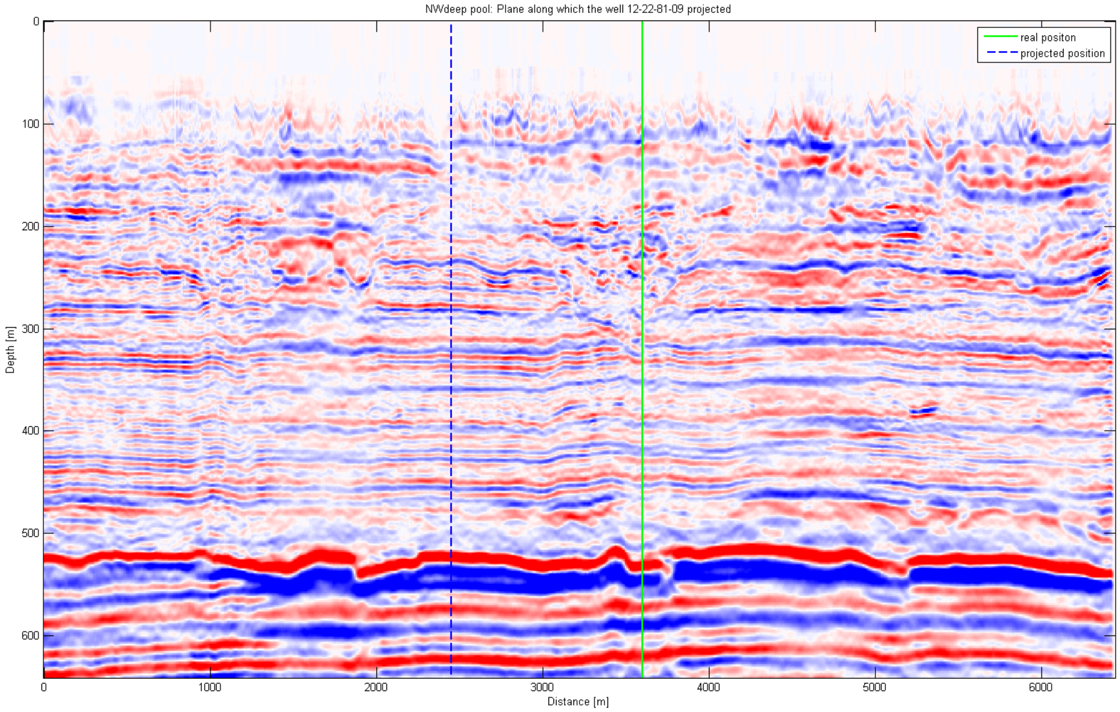

Figure B.8: Cross section along well 1222 and its projected position.

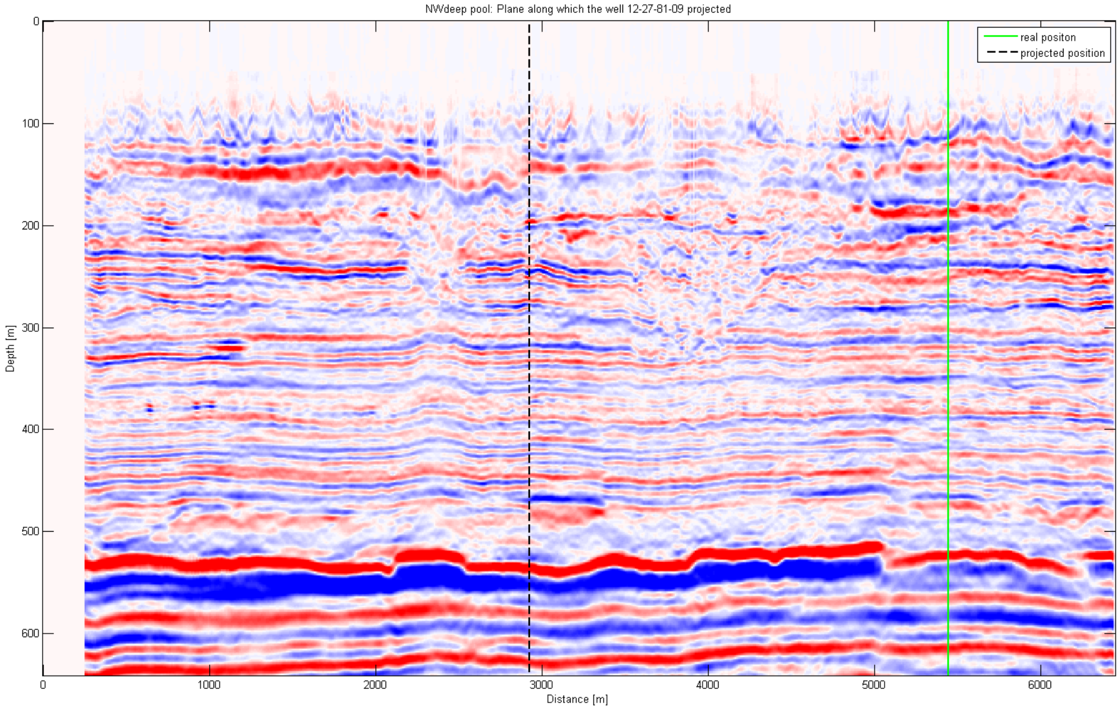

Figure B.9: Cross section along well 1227 and its projected position.